Carolina Gomes Morgado

Bachelor of Science in Micro and Nanotechnology Engineering

Stacks of alternating conductive and non-conductive oxides for controlling electric fields at a spatial resolution of 100 nm in the core of a waveguide

Dissertation submitted in partial fulfillment
of the requirements for the degree of

Master of Science in
Micro and Nanotechnology Engineering

Adviser:	Prof. Jan Genoe, Full Professor, University of Leuven
Co-adviser:	Prof. Elvira Fortunato, Full Professor, NOVA University of Lisbon

Examination Committee

Chair:	Prof. Hugo Águas
Rapporteurs:	Prof. Pedro Barquinha
	Prof. Elvira Fortunato

FACULDADE DE
CIÊNCIAS E TECNOLOGIA
UNIVERSIDADE NOVA DE LISBOA

January, 2020

Stacks of alternating conductive and non-conductive oxides for controlling electric fields at a spatial resolution of 100 nm in the core of a waveguide

This document was created using the (pdf)LaTeX processor, based on the "novathesis" template[1], developed at the Dep. Informática of FCT-NOVA [2].
[1] https://github.com/joaomlourenco/novathesis [2] http://www.di.fct.unl.pt

"This is Major Tom to Ground Control,
I'm stepping through the door,
And I'm floating in a most peculiar way,
And the stars look very different today".
- David Bowie

Acknowledgements

This space will be used to express gratitude to a large group of people who helped me achieve a personal and professional growth.

Gostaria de começar por agradecer à minha co-orientadora e Professora Elvira Fortunato, por me ter proporcionado uma experiência impressionante e que, durante o decorrer da tese, sempre se demonstrou disponível para me ajudar e aconselhar. Estendo este agradecimento ao Professor Rodrigo Martins que conjuntamente com a Professora Elvira, criou o inovador curso de Engenharia de Micro e Nanotecnologias, do qual me orgulho tanto de pertencer.

I'd like to share my gratitude towards my supervisor Professor Jan Genoe, for accepting me in his project and trusting me to bring innovative work to the team. Additionally, thanks to him, Prof. Elvira Fortunato and Prof. Paul Heremans, I was able to experience one of the best research centers in the world - *imec*. A deeply thank to the *Video-Holographers* for being always there when I needed guidance - Dr. Robert Gehlhaar, Dr. Manoj Nag and Dr. Cédric Rolin. A special appreciation to Guillaume, my co-co-supervisor who guided throughout the process and was always willing to help me, even several times a day. To all the LAE deparment for the friendship and the inclusiveness from day one until departure.

Leuven brought me unforgettable professional and life experiences, but nothing compares with the memories I shared with my friends. It's amazing to know some people will stay in our lives forever - Monse, Marios, Gustavo, Lauriña, thank you for your friendship and craziness during this period. Azamat, Mohammed, Matos, Rossa, Gema and Mauricio, thank you for being the lunch crew inside imec, but also the amazing friends after office hours. Konstantina and Marios, thank you so much for your friendship and companionship during my stay in Belgium, you are fantastic friends. Thank you Maria and Giulia, for making me believe that distance is nothing when someone means so much.

Ao meu amigo e ex-colega de casa, Manuel Matos, pela grande amizade e paciência que tiveste para mim durante estes 5 anos de curso. E o resto já disse na fita de finalista, por isso fiquemos por aqui!

À Mónica pelos 500.000 filmes que assistimos no cinema nos últimos anos, por aqueles que vimos por duas vezes, pelas mil séries que discutimos em conjunto e por todos os livros que me emprestaste e que eu nunca li. Só não posso agradecer mais, porque ainda não viste o Outlander. Mas bem, agradeço pela amizade única e verdadeira que me proporcionas diariamente. À Andreia e ao Ruben por serem pilares constantes na minha vida. Um agradecimento especial à Andreia pela amizade, carinho, desabafos e repreensões. És e sempre serás a irmã que nunca

tive! Agradeço ainda ao meu irmão, por ser uma pessoa tão pura e minha amiga.

Agradeço ao meu tio Paulo, por ser o meu ídolo e uma wikipedia humana. Ao meu tio Ruy, por todo o carinho que me deu. Aos meus queridos avós, por serem os meus melhores amigos e significarem tanto para mim. Sem vocês, nada seria possível. Obrigada por serem as melhores pessoas que alguma vez conheci e por me fazerem acreditar que o amor verdadeiro existe. Um agradecimento especial ao meu avô, por ter sido um pai para mim, por me ter ido buscar à escola, sendo ela localizada a 5 min da sua casa, ou a 1 hora.

Aos meus pais, por serem quem são e por me terem proporcionado tudo o que tive até hoje. Não são quaisquer pais que deixam a filha de 10 anos ir sozinha para o Bairro Alto estudar dança no conservatório, por ser o sonho dela; ou que a deixam participar em teatros, tendo de assistir a estes 20 vezes num espaço de 3 meses. Sem eles, não teria a possibilidade de dizer que já vivi em 3 países estrangeiros, nos quais aprendi e cresci tanto. Por todo o amor incondicional e aprendizagens ao longo da vida, um eterno obrigada!

Ao Tó, por tudo o que me proporcionas diariamente. Por todas as memórias que partilhamos e que só nós as sabemos. Por todo o amor, carinho e devoção. Sem ti, nada seria igual... Um grande obrigada.

Abstract

Holography is a revolutionary display technology capable of creating a true three-dimensional (3D) image. In Hollywood movies such as "Star Wars", advanced holograms at video-rate are often present and appreciated by the audience. Unfortunately, despite many efforts from the scientific community, fast rewritable high-quality holograms haven't been created yet.

This work focuses on developing a structure capable of bringing this type of holography to life. To achieve this, a slab waveguide is proposed, where the core contains an electro-refractive material. By applying local electric fields with analog control and nano-precision inside the core, its refractive index will change locally. Light traveling along the core, when encountering the affected area, will be leaked into free space and create a hologram. These electric fields will be controlled through one of the conductive pillars of the cladding structure. For the latter, a novel metamaterial is being developed and this work centers on its optimization.

For this, transparent conductive oxides (TCO) will be used, as metals will lead to parasitic scattering and absorption of light in the cladding. Hence, the optical properties of the alternating conductive and non-conductive oxide pillars of Indium Gallium Zinc Oxide (IGZO) and Silicon-Oxy Nitride (SiO_xN_y), respectively, need to be matched. In this study, the refractive index and extinction coefficient of both materials have been determined by spectroscopy ellipsometry (SE) and compared. IGZO pillars were created by optical photolithography and the appropriate etch time was optimized. Finite-difference time-domain (FDTD) simulations were carried out to be compared with future practical results of the structure altogether.

Keywords: Video-rate holography; Rewritable holograms; IGZO; SiO_xN_y; Metamaterial; Slab Waveguide; Analog control; Optical properties; Optical photolithography; FDTD simulation

Resumo

Holografia é uma tecnologia de display revolucionária, capaz de criar uma imagem verdadeiramente tridimensional (3D). Em filmes de Hollywood, tal como a "Guerra das Estrelas", estão presentes hologramas avançados com taxa e qualidade de vídeo, sendo bastante apreciados pela audiência. No entanto, apesar de inúmeros esforços por parte da comunidade científica, hologramas rápidos, regraváveis e de alta-qualidade ainda não foram realizados.

De modo a obter tais hologramas, este estudo propõe a utilização de um guia de onda planar, no qual o núcleo é composto por um material electro-óptico. Através de um controlo analógico e nano-preciso, um campo eléctrico é aplicado. Isto irá desencadear a modificação local do índice de refracção dentro do núcleo. Se uma luz estiver a viajar dentro deste e encontrar uma zona afectada, irá escapar para o ar, criando um holograma. Estes campos eléctricos são controlados através de pilares condutores existentes na casca do guia de onda. Para tal, um metamaterial inovador está a ser desenvolvido, sendo que este trabalho foca-se na sua optimização.

Foram utilizados óxidos transparentes condutores, uma vez que os metais criam dispersão e absorção parasítica da luz que viaja dentro do núcleo. Pela mesma razão, é necessário igualar as propriedades ópticas dos pilares alternos de materiais condutores e não-condutores, compostos por óxido de zinco gálio índio (IGZO) e oxinitreto de silício (SiO_xN_y), respectivamente. Neste estudo, os índices de refracção e os coeficientes de extinção de ambos os materiais serão determinados e comparados através da espectroscopia elipsométrica (SE). Os pilares condutores de IGZO foram paternizados através da fotolitografia óptica e o tempo de corrosão química foi optimizado. Foram realizadas simulações que utilizam o método de diferenças finitas no domínio do tempo (FDTD) de modo a serem comparadas com futuros resultados práticos.

Palavras-chave: Holografia com taxa de vídeo; Hologramas Regraváveis; IGZO; SiO_xN_y; Metamaterial; Guia de onda planar; Controlo analógico; Propriedades ópticas; Fotolitografia óptica, Simulação FDTD;

Contents

List of Figures

List of Tables

Acronyms

2D	Two-dimensional
3D	Three-dimensional
AFM	Atomic Force Microscopy
a-IGZO	Amorphous Indium Gallium Zinc Oxide
BC	Boundary Conditions
BTO	Barium Titanate
CGH	Computer-Generated Hologram
DC	Direct Current
DIW	Deionised Water
EBR	Edge Bead Remover
ERC	European Research Council
FDTD	Finite-difference time-domain
GST	Germanium Antimony Tellurium Alloy
ICP-CVD	Inductively Coupled Plasma Chemical Vapor Deposition
IGZO	Indium Gallium Zinc Oxide
IO	Insulating Oxide
ITO	Indium Tin Oxide
MOSFET	Metal-Oxide-Semiconductor Field Effect Transistor
MSE	Mean Squared Error

PCM	Phase-change Material
RC2	Dual Rotating-Compensator
RCE	Rotating-Compensator Ellipsometer
RGB	Red Green Blue color model
SE	Spectroscopic Ellipsometry
SEM-FIB	Scanning Electron Microscope - Focused Ion Beam
TARC	Top Anti-Reflective Coating
TCO	Transparent Conductive Oxides
TFT	Thin Film Transistor
TMAH	Tetramethylammonium Hydroxide
TSO	Transparent Semiconductive Oxide
UV	Ultraviolet

Symbols

A	Transition matrix parameter
α	Absorption coefficient
Ar	Argon
$BaTiO_3$	Barium Titanate
C	broadening term
Δ	Phase difference between s- and p- light waves
δ_{rp}	Phase of p- polarized light upon reflection
δ_{rs}	Phase of s- polarized light upon reflection
δ_x	Initial phase of the electric field in the x direction
δ_y	Initial phase of the electric field in the y direction
E	Photon energy
E_0	Peak transition energy
E_g	Band gap energy
$\epsilon_r(w)$	Complex relative dielectric constant
E_x	Electric field in the x direction
E_{x0}	Wave amplitude in the x direction
E_y	Electric field in the y direction
E_{y0}	Wave amplitude in the y direction
$\hat{x}$	Unit vector in the x direction
$\hat{y}$	Unit vector in the y direction
ε_2	Imaginary part of the complex dielectric constant
ε_{2L}	Imaginary part of the complex dielectric constant from the Lorentz oscillator model

ε_{2TL}	Imaginary part of the complex dielectric constant from the Tauc-Lorentz model
k	Extinction coefficient
K	Propagation number
λ	Wavelength
$LiNbO_3$	Lithium Niobate
n	Refractive index
N	Complex refractive index
N_2	Nitrogen
N_2O	Nitrous Oxide
O_2	Oxygen
π	The numerical value of pi
Ψ	Amplitude ration
ε_1	Real part of the complex dielectric constant
ε_{1TL}	Real part of the complex dielectric constant from the Tauc-Lorentz model
R_p	Fresnel reflection coefficient for p- poralized light
R_s	Fresnel reflection coefficient for s- poralized light
Si	Silicon
Si_3N_4	Silicon Nitride
SiH_4	Silane
SiO_2	Silicon Oxide
SiO_xN_y	Silicon Oxy-Nitride
Ti	Titanium
t	Time
ε	Complex dielectric constant
$\vec{D}$	Displacement field
$\vec{E}$	Electric field
$\vec{H}$	Magnetic field

w Angular Frequency

Chapter 1

Motivation and Objectives

Almost 50% of the human's brain is used to perceive visual information [1]. Visualization is then, an extremely vital concept and in the current world, nearly all content is delivered to us through a screen. Hence, since the introduction of the display technology, civilization is constantly searching for a better screen device. Accordingly, 3D display technologies are gaining importance day by day. Holography was invented in 1947 by Gabor and creates a true 3D image. This is possible because a hologram records all features of a light wave - phase, amplitude and wavelength. Therefore, this technology is considered to be the "holy grail"of 3D. Although it has been widely investigated by researchers, a high-quality rewritable hologram at video-rate hasn't been created yet. Optically rewritable holograms have been developed using photo-refractive crystals. However, its slow response time and narrow number of reading cycles make them unfit for video-rate holography. Acoustically rewritable holograms have a fast response but can't generate complex images.

This study is part of an European Research Council (ERC) project led by Prof. Jan Genoe that is determined to develop a promising slab waveguide able to generate fast and complex holograms. The latter will be created through evanescent leaky waves from the core of the waveguide and will be controlled through a local change of the core's refractive index. This local change is caused by electric fields applied with analog control and nano-precision through one of the conductive pillars of the cladding [2]. The cladding structure is made of alternating conductive and non-conductive oxide pillars. The objective is to match the refractive indices of both materials so light traveling along the core doesn't experience any deviation. This study is centered on the optimization of the cladding metamaterial and the workload is as follows:

- Deposit layers of SiO_xN_y by Inductively Coupled Plasma Chemical Vapor Deposition (ICP-CVD) on Si wafers, and IGZO by Direct-Current (DC) Sputtering on Si wafers.
- Pattern IGZO films using photolithographic processes. Then, determine the optimized etch time for the deposited thicknesses, by characterizing the samples using AFM, SE and profilometry.
- Compare the optical properties of both materials, which were determined by SE.
- Carry out FDTD simulations on Lumerical, as a preliminary study of how the cladding grating structure behaves with light.

2.1 Holography Background

From conventional photography to state-of-the-art displays, there is a desire to represent reality as much accurately as possible. Living in the 21^{st} century is synonym to being surrounded by information and entertainment through a screen. Yet, most of the current displays only show two-dimensional (2D) pictures and films, missing depth information [1]. Thus, 3D stereoscopic display devices have been developed, stimulated by the urge to convey this depth perception to the viewer. This technology is present in several fields, such as video-gaming, augmented reality, aerospace, medicine and motion picture. Nonetheless, calling this technique realistic 3D is a fallacy, since the image created is nothing but an illusion of depth to the human eye. A 3D stereo film is also dependent on eyeglasses and is often related to headaches and nausea, due to the conflict between some depth key features in a human brain.

In order to comprehend physical depth, the brain needs to perceive some cues, such as convergence, motion parallax and binocular disparity [1]. The ultimate goal is the artificial creation of these features/effects which is possible through holography, opening the pathway to the creation of a true high-resolution 3D image.

Holography is not a recent term, since it was invented 72 years ago by Dennis Gabor while improving the electron microscopy resolution. The word originates from the Greek words *holos* and *graphos* which means *the complete writing*. This is a rational term, since an hologram records the whole information of an object [3].

A traditional photograph is a 2D image of an object because it only records the amplitude or the intensity distribution of the light waves [4]. In a hologram, both the intensity and the phase are recorded, therefore containing all optical information [3].

The recording of a hologram can be understood by looking at the phenomenon of interference [4]. As represented in Figure 2.1a, a relatively simple optical setup consisting of a coherent light source, a beam splitter, an object and a photographic plate can record a hologram. A coherent beam emanates onto a beam splitter, which divides the light beam into two - one is reflected and the other is transmitted. The prior is deviated to the photographic plate, serving as the reference ray. The latter strikes the photographic plate after being reflected from different points of the object's surface. Hence, it is often called the object ray. When reaching the photographic plate, both beams will interfere with each other, and their superposition will create an interference pattern at the photographic plate, which D. Gabor [3] called a hologram.

After the recording of the hologram, one is left with an optical code with no visual meaning.

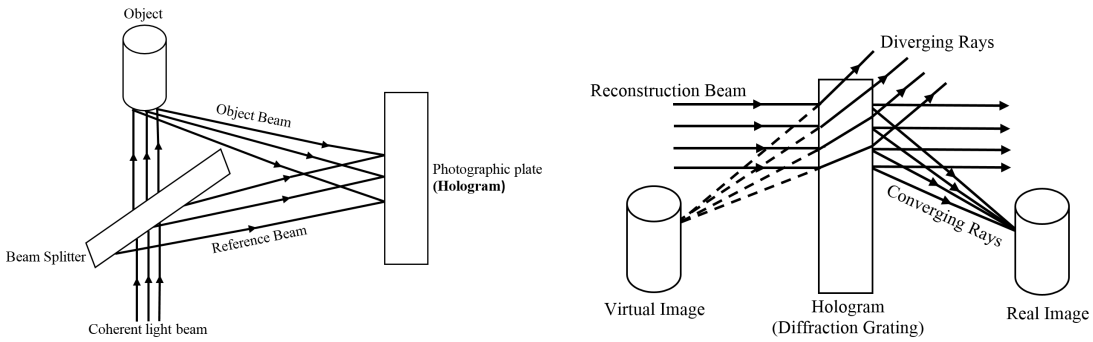

(a) (b)

Figure 2.1: Adapted from [4], figure (a) shows the recording process of a hologram, and (b) its reconstruction.

Therefore, the process of reconstruction is needed. As represented in Figure 2.1b, it consists of shining a coherent beam identical to the reference ray onto the hologram [5]. The latter will act as a diffraction grating producing a real and a virtual images of the object. Both images are on the same axis, but separated by the hologram [6]. When trying to focus on one image, Gabor could encounter some disturbances, since the other one could still be seen out-of-focus [3, 6]. This aberration was corrected in 1962, when the laser became available, producing a much more coherent beam than a mercury lamp. This was accomplished by Leith and Upatnieks, which were able to separate these two images in different angles. Therefore, a viewer could focus on one single image and see the true copy of the object [1, 5]. If a viewer looks at the image from various angles, they will see it in different perspectives. This wasn't possible with a regular 3D stereoscopic display and thus, holography is considered by many to be the holy grail of the 3D technology.

2.2 Breakthrough Innovation

Holography has evolved over the last 70 years from static monochromatic 3D images to rewritable full-color 3D images. However, video-rate switchable holograms haven't been realized yet. Several projects focusing on optical and acoustically rewritable holograms came close to this goal, but still have some imperfections [3].

Optically rewritable holograms can be generated using photo-refractive crystals, such as doped lithium niobate ($LiNbO_3$). When two laser beams - a signal and a reference, are incident upon this material, their interaction creates an interference pattern. Electrons excited by light will migrate to the dark fringes and get trapped there in deep states. These unbalanced charges create a space-charge field, locally modulating the refractive index through the electro-optic effect. Later, when a "reading" laser ray strikes the material again, the storaged optical code will create an image [5, 7, 8]. This is a clever way to produce a high-quality hologram, since it presents great spatial resolution - up to 10 000 lines per *mm*. Moreover, it is a great solution for optical data storage due to its long retention time. Nevertheless, this technology has several drawbacks

for video-rate holography such as slow response time, limited number of reading cycles and high energy consumption [7, 9].

Acoustically rewritable holography is a more recent concept which consists in the local modulation of the refractive index of a $LiNbO_3$ waveguide with the use of acoustic waves. This has been proved to be a very fast process, as it is able to rapidly switch from one image to another, therefore having the temporal resolution for video-rate holography. Unfortunately, the complexity of the said images is very narrow due to the periodicity of the acoustic waves, closing the window to any other patterns [10].

A pioneering idea is proposed by the ERC Project named "Video-rate holographic projection by novel metamaterials" granted to my supervisor Prof. Jan Genoe, that aims to create fast electrically-controlled switchable holograms that also are able to generate elaborated images [2].

In principle, this can be realized with a structure similar to the one represented in Figure 2.2a. An electro-refractive material, such as barium titanate - $BaTiO_3$ or BTO, is used as the core of a slab waveguide. It is known that the refractive index of materials with large crystals, such as $BaTiO_3$ or $LiNbO_3$, can be modulated at high speed, in the order of sub-nanoseconds. This is accomplished by applying a local electric field, making them ideal to be used in electro-optic modulators [11]. These local electric fields need to be controlled with high precision which will be achieved by the bottom cladding consisting of a novel metamaterial.

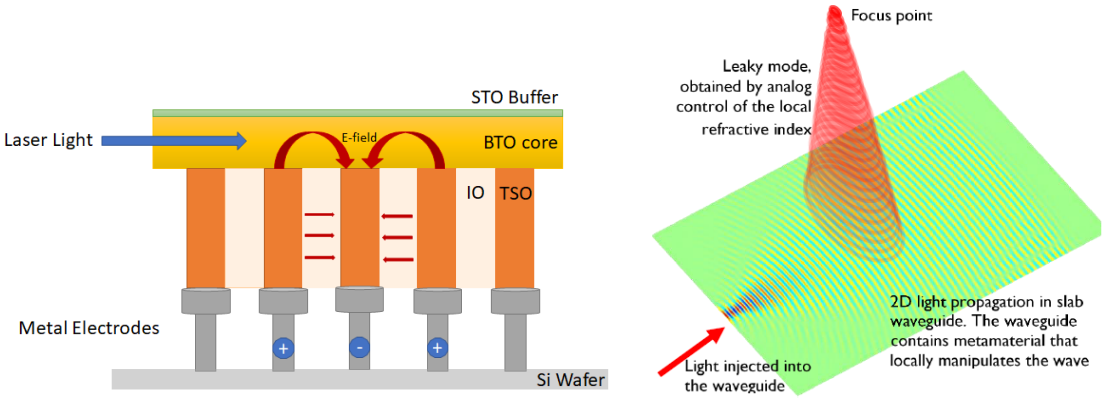

(a) (b)

Figure 2.2: (a) Configuration of the envisioned project for producing electrically-controlled holography. The cladding consists of alternating isolating oxides (IO) and transparent semiconductor oxides (TSO). (b) generation of a hologram through leaks of the light propagating in the core of a waveguide. Adapted from [2]

The bottom cladding consists of pillars of alternative conductive and non-conductive oxides with almost identical optical properties and therefore optically acts as a single material. These pillars have a high aspect ratio (3 to 15), their size is sub-wavelength (25 to 50 nm) and have a period ranging from 50 to 100 nm. The conductive oxide arrays are connected to metal electrodes below to make a connection to the silicon driving electronics. As shown in Figures 2.2a and 2.2b, if a coherent beam, such as a laser, is injected into the BTO core, it will suffer a deviation when encountering a local electric field. This is because the local electric field causes an alteration

on the BTO refractive index. In turn, the electric field generated between two pillars originates from a voltage difference applied by the metal electrodes. The sub-wavelength size of the pillars ensures that one can have complete control over any sort of light used, achieving 50 *nm* resolution. This is the unique and breakthrough advantage of the proposed project - it conjugates high speed with an analog control. Subsequently, complex images can be created at video-rate. Furthermore, in order to create a RGB image, the refresh rate needs to reach the GHz.

This thesis is focused specifically on the optimization and designing of the cladding metamaterial and therefore there will be no further mention to the electrical control of the pillars or the development of the core BTO.

Since the light needs to be precisely maneuvered and should stay inside the core, no scattering or absorption should occur along the way. Hence, transparent semiconductive and isolating materials are the best option for the cladding, such as Nitrides and Oxides. The underlying metal electrodes can be a prime source of parasitic scattering and reflection of light. To avoid this, the thickness of the cladding should be at least 400 to 500 nm.

The material of choice for the conductive oxide pillars is Amorphous Indium Gallium Zinc Oxide (a-IGZO), which is a Transparent Semiconductive Oxide (TSO). a-IGZO has been widely developed over the past two decades and is mainly used for the fabrication of Thin Film Transistors (TFTs) which are an alternative to the classic Metal-Oxide-Semiconductor Field Effect Transistor (MOSFET) [12, 13]. Even though this material is still rather unknown for optical and plasmonic applications [14], it presents the best properties due to its refractive index over the visible range ($n = 1.8 - 1.9$), very low absorption coefficient, α, (or extinction coefficient - k) and can be easily depleted of carriers [15].

For the insulating oxide (IO) pillars, SiO_xN_y is the chosen material. It consists of a mixture of silicon nitride, Si_3N_4, and silicon oxide, SiO_2. This material has been extensively studied for optical devices due to its low-cost and great reproducibility. The greatest advantage is the tunability of its refractive index, ranging from 1.45 to 2 [16]. The right amount of each compound will create a refractive index identical to of the a-IGZO. If this is accomplished, the cladding will behave as one single material and light traveling along the core won't be scattered. Moreover, as the pillars have a sub-wavelength size, the cladding structure will act as a metamaterial. The latter is a man-made material that presents sub-wavelength patterns of different compounds. For this reason, it acts as an homogeneous medium with effective electromagnetic properties and consequently the effective medium approximation can be considered, i.e. its properties solely depend on the growth conditions, its structure and composition [17].

2.3 Competitive Ideas

Another approach has been tried to create dynamic high-quality holographic images. Rewritable full-color computer generated holograms (CGHs) have been developed. For this, a phase-change material (PCM) - Germanium Antimony Tellurium alloy (GST) is used. Through an external stimuli, GST undergoes a phase-change from amorphous to crystalline at $150°C$. This leads to a notable change, within the visible range, of the refractive index and extinction coefficients of the

material. Furthermore, this change is non-volatile, reversible, and controlled by either an optical and electrical stimuli [18, 19].

GST is kept between Indium Tin Oxide (ITO) layers, as the ITO upper layer is protecting the former from oxidation. A mask with a CGH pattern, with a pixel pitch of 1 μm and a 16k × 16k resolution is attached to this structure [18]. The process consists in illuminating this mask with a laser. The pattern will be engraved in the GST layer and can be later reconstructed to create a hologram [18, 19].

2.4 Spectroscopic Ellipsometry

2.4.1 Basic principles

SE is an extremely accurate, sensitive and non-destructive optical measurement technique that exploits the fact that there is a change of the polarization state of light after being reflected from a surface. This phenomenon can be used to determine thickness and optical properties of thin films, bulk and multilayer structures [20, 21].

As once stated by Maxwell, light waves have electromagnetic behavior being composed of an electric field traveling orthogonally to a magnetic field. The direction in which the electric field vector is oscillating, as a function of space and time, is defined as polarization [22]. A regular beam of light is composed of several light waves with arbitrary electric field directions. Therefore, this type of source is unpolarized.

When electromagnetic waves are oscillating in the same direction, the light is polarized. The latter can be defined by superimposing two electric fields, E_x and E_y, traveling in the x and y directions, respectively [20]. Therefore, one can describe the sum of these two light waves, as an electric field traveling in the z-direction, as expressed in Equation 2.1:

$$E(z,t) = \left\{E_{x0}\, e^{i(wt-Kz+\delta_x)}\right\}\hat{x} + \left\{E_{y0}\, e^{i(wt-Kz+\delta_y)}\right\}\hat{y} \tag{2.1}$$

where $\hat{x}$ and $\hat{y}$ are assumed to be unit vectors in the x and y directions, respectively, E_{x0} and E_{y0} are the wave amplitudes in the x- and y- directions, w is the angular frequency, t is the time, K is the propagation number and δ_x and δ_y are the initial phases of both x- and y- electric fields, respectively. These electric fields are characterized by their initial amplitude, initial phase and wave numbers [20].

One should consider a case of $E_{x0} = E_{y0}$ and $K = 1$. If the phase difference $(\delta_x - \delta_y)$ between these two electric fields is a multiple of $\pm\,\pi$ [23], the resultant wave is said to be linearly polarized. If the phase difference is different than zero, the resultant vector rotates elliptically in the $x - y$ plane while the wave is propagating [20]. Another particular case occurs when the phase difference is a multiple of $\pm\,\frac{\pi}{2}$ and the light becomes circularly polarized. Elliptical polarization can be achieved if linearly polarized light is reflected from a surface and if certain conditions are encountered [21]. Figure 2.3 shows a representation of both elliptical and linear polarizations.

When light is reflected or transmitted at an interface, it becomes polarized in a certain way depending on the state of polarization of the incident light and the incident angle [21]. In other

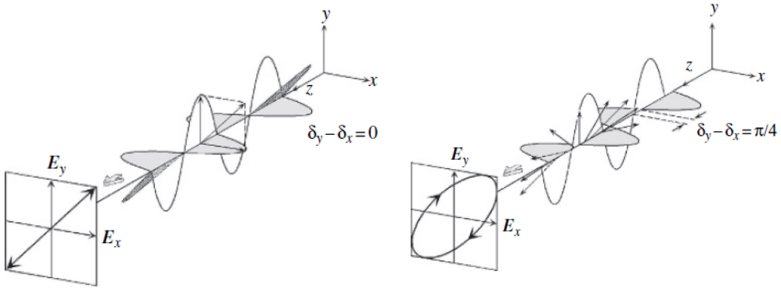

(a) (b)

Figure 2.3: Representation of both (a) linear polarization, when the phase difference between two electric fields is 0 and (b) elliptical polarization, when the phase difference is $\frac{\pi}{4}$ [20].

terms, there is a phase change of both parallel, p, and perpendicular, s, electric fields in respect to the light's plane of incidence [23].

Numerous optical configurations are available for SE. When using a Rotating-Compensator Ellipsometer, (RCE), a completely unpolarized light source is used. A polarizer is placed in front of the source, transmitting linearly polarized light. When in-phase s- and p-polarized light waves are illuminated on the sample, typically at the Brewster angle [20], elliptically polarized s- and p- light waves are reflected from it completely out of phase. A rotating-compensator is placed firstly, followed by an analyzer and a detector, represented in Figure 2.4:

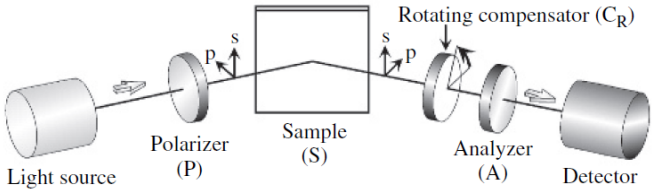

Figure 2.4: Optical configuration of a RCE (PSC_RA) [20].

SE indeed measures the phase difference between s- and p- light waves, Δ, and the change in the ratio of their amplitudes, $\tan\Psi$, upon reflection [23] is defined by Equations 2.2 and 2.3:

$$\Delta = \delta_{rp} - \delta_{rs} \tag{2.2}$$

$$\tan\Psi = \frac{|R_p|}{|R_s|} \tag{2.3}$$

where δ_{rp} and δ_{rs} are the phases of p- and s- polarized electric fields upon reflection, respectively. R_s and R_p are known as the Fresnel reflection coefficients for both parallel and perpendicular polarized light, respectively. These are defined as the ratio of the reflected electric fields to incident electric fields and are usually complex numbers.

The ellipsometric parameters (Ψ,Δ) are related to the Fresnel reflection coefficients. This relation is called the *Fundamental Equation of Ellipsometry* [21] and is given by Equation 2.4:

$$\rho = \tan\Psi \exp(i\Delta) = \frac{R_p}{R_s} \tag{2.4}$$

When considering a simple structure of an isotropic and homogeneous material, the amplitude ratio, Ψ, is related to the refractive index, n, whereas the phase difference, Δ, is related to the amount of light that is absorbed, which is described by the extinction coefficient, k. Therefore, two important parameters, (n,k) can be provided by SE, leading to an easy determination of important properties such as the complex refractive index, $N \equiv n - ik$, the complex dielectric constant, $\varepsilon = N^2 = \varepsilon_1 - i\varepsilon_2$, where ε_1 and ε_2 are their real and imaginary parts, respectively; and the absorption coefficient, $\alpha = \frac{4\pi k}{\lambda}$, where λ is the wavelength of light [20, 21].

2.4.2 Modeling and Fitting

SE is an indirect characterization technique and therefore leans on theoretical models to accurately analyze the data. The analysis consists of three significant steps: modeling of a dielectric function, defining of an optical model and fitting this model to the SE data [20].

In previous works, the Tauc-Lorentz model has been applied to determine the dielectric function of amorphous materials. In recent studies, it has been widely utilized for the determination of the dielectric function of TCOs and TSOs [20]. The imaginary part of the dielectric function, ε_{2TL}, is given by the product of the Tauc joint density of states and the imaginary number ε_{2L} derived from the classic Lorentz oscillator model [24, 25], given by Equation 2.5:

$$\varepsilon_{2TL}(E) = \begin{cases} \frac{AE_0C(E-E_g)^2}{(E^2-E_0{}^2)^2}\frac{1}{E} & E > E_g \\ 0 & E \leq E_g \end{cases} \tag{2.5}$$

where E_0 is the peak transition energy, E_g the band gap energy, A the transition matrix parameter and C the broadening term. These are treated as fitting parameters and are a function of the photon energy, E. The Kramers-Kronig integration allows for the correlation between ε_{2TL} and the real part of the dielectric function, ε_{1TL}.

It is essential to quantify how much the acquired data fits to the chosen model. The error estimator used in this work is the mean squared error (MSE), which quantifies the sum of the squares of the differences between the model set up data and the measured data [20]. Hence, the model can be either accepted or refused through this value. The smaller the MSE, the better the fitting [26]. For simpler structures, such as bare Si substrates, the MSE value can be as small as 1. For more complex structures, such as multilayers, the value can be larger than 10 and considered acceptable [26].

Chapter 3

Methodology

This chapter summarizes the processes of fabrication, optimization and characterization of the cladding structure.

3.1 Deposition Techniques

3.1.1 Direct Current (DC) Sputtering

The first step was to properly clean bare Si wafers. This was followed by the deposition of 100 and 200 nm a-IGZO films using a DC sputtering *"Leybold System"*. The process was done at room temperature with a ceramic target ratio of $1:1:1:4$ and a sputter power of 1600 W. The films were deposited in an ambient combination of argon Ar and oxygen O_2. A small amount of O_2 is recommended in order to have a better control of the stoichiometry of the a-IGZO films. This system allows a maximum of 8 wafers in the substrate holder. The latter is placed under the target and is kept at constant movement in order to improve the deposition uniformity. The speed and the number of passes of the holder is controlled in order to obtain the desired thickness [27].

3.1.2 Inductively Coupled Plasma Chemical Vapor Deposition (ICP-CVD)

The second step was to deposit SiO_xN_y layers on bare Si wafers, as one is interested in determining its optical properties. SiO_xN_y was deposited on five Si wafers at 150°C and 2000 W by ICP-CVD. Three different gases, nitrogen N_2, silane SiH_4 and nitrous oxide N_2O were mixed inside the chamber, while the pressure was varied between 7 - 9 $mTorr$. The process took approximately 20 minutes, so a film of 200 - 250 nm was expected. Even though the gas flow rates for SiH_4 and N_2 were kept the same for all samples, the amount of N_2O was varied from 2 - 6 sccm, with steps of one unit, to change the refractive index of the material. Table 3.1 shows the gas flow rates used for each component.

Table 3.1: Gas flow rates used for each component inside the ICP-CVD chamber.

	SiH_4	N_2O	N_2
Gas Flow Rate (sccm)	16.6	2.0 - 6.0	13.3

3.2 Creation of a Grating Structure

3.2.1 Mask Design

A quartz mask was previously designed containing regions of different grating sizes, represented in Figure 3.1. Each region was labeled from $F1$ - $F5$, with sizes descending from 10 - 1 μm. Table 3.2 expresses the size of each grating region. There are four unlabeled regions in every corner of the mask containing Fresnel lenses. Each region is subdivided in four areas with different grating directions. Figure 3.2 represents one of these regions with the four grating orientations.

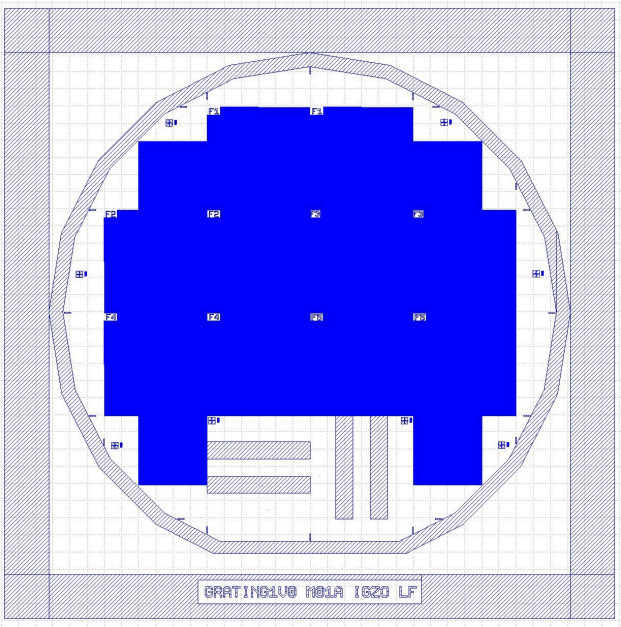

Figure 3.1: Template of the designed mask used for the photolithographic process.

Table 3.2: Grating sizes of each region located in the mask.

	Region				
	$F1$	$F2$	$F3$	$F4$	$F5$
Grating Size	10 μm	7 μm	5μm	3 μm	1 μm

Prior to use, the mask was submitted to a standardized cleaning protocol with acetone, $MicroStrip$2001 at 30$^{\circ}C$, isopropanol and deionised water (DIW).

3.2.2 Optical Photolithography

Optical photolithography was performed in order to pattern the a-IGZO. Two distinct recipes were experimented, differing on the used resist, spinner and mask aligner tool.

The first recipe begins with the coating of the samples with titanium (Ti) prime, an adhesion promoter that improves the resist adherence on Si substrates. $IX845G$ positive resist that develops in common tetramethylammonium hydroxide (TMAH) based developers was deposited on top.

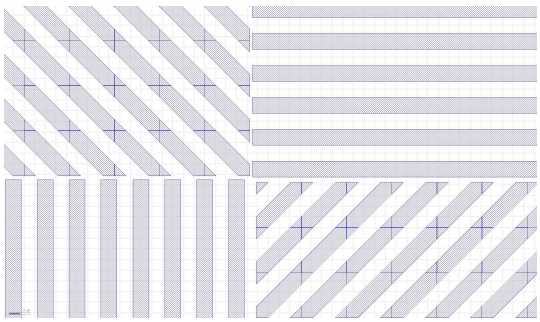

Figure 3.2: Representation of one of the grating regions, which are subdivided into four parts. Each part has a different grating direction.

Both were deposited using a $WS - 6501$ spinner equipment *"Laurell Technologies Corporation, USA"* at 4000 rpm for 30 seconds followed by a soft-bake at $120°C$ for 1 minute. The samples were exposed to ultraviolet (UV) light using a *Süss MA*6 mask aligner. After the exposure, the samples were developed for 1 min on a TMAH based developer (industry designation: *OPD* 5262), provided by *Fujifilm*.

The second recipe utilizes a state-of-the-art spinner, *Süss Delta* 80, that is based on the *GYRSERT* technology. The latter uses a closed cover when rotating the substrate that will allow for a reduced usage of the resist and a better uniformity of the film [28]. A Ti prime coating is first done at a rotating speed of 2000 rpm for 30 seconds, followed by a soft-bake at $120°C$ for 90 seconds. Next, a positive resist, *AZ ECI* 3012, is deposited at 4800 rpm for 30 seconds, followed by a soft-bake at $100°C$ for 90 seconds.

The wafers are also coated with a top anti-reflective coating (TARC). As it will be explained below, these samples will be exposed with monochromatic light. Although this improves the control of the process and allows smaller features, it has a disadvantage - it can easily create interferences between the incident and reflected lights during the exposure. The TARC *AZ Aquatar Solution* will significantly reduce this effect. It is spinned over the photoresist at 1750 rpm for 30 seconds [29].

Spinner *Delta* 80 includes a fully programmable and automatic Edge Bead Remover (EBR) option, that removes the resist from the edges of the wafer [28]. This will improve thickness uniformity, as there might be excess resist on the edges. The solvent used is the *RER* 500 provided by *Fujifilm*.

The exposure step typically uses a broadband UV exposure, with a wavelength range between 300 - 450 nm. Although, depending on the sensitivity of the used resist, one can choose to expose it to a monochromatic light. For this work, i-line exposure was selected, that exposes to a wavelength of 365 nm. This was performed using a *Süss MicroTec MA*8 mask aligner. After the exposure, the samples were developed for 1 min on *OPD* 5262.

Afterwards, all samples underwent a wet etching using 5% oxalic acid. Table 3.3 outlines the etch times used on 100 and 200 nm a-IGZO films. All samples were rinsed in DIW for 5 minutes. Finally, they were bathed in acetone in an ultrasonic bath for 10 minutes to remove the unexposed resist.

Table 3.3: Etch times experimented on 100 and 200 nm a-IGZO films in order to optimize the patterning.

100 nm a-IGZO	200 nm a-IGZO
2 min	3 min
2:30 min	5 min
3 min	7 min
3:30 min	9 min

3.3 Characterization Techniques

3.3.1 Grating Characterization

Topographic images were acquired on tapping mode from a *Bruker Atomic Force Microscopy Dimension Edge Scanner, NanoDrive v*8.06 and treated with *Gwyddion* software. From these images, profiles were extracted along arbitrary lines, in order to determine the thickness and the appropriate etch time. Profiles were collected using a *Bruker DEKTAK XT Stylus* profilometer on contact mode for comparison purposes.

3.3.2 Spectroscopic Ellipsometry

As one is interested in determining the optical properties and the thicknesses of both deposited films, SiO_xN_y and a-IGZO, SE measurements were performed on a *J. A. Woollam Dual Rotating-Compensator (RC2) SE*. The analyzer was kept at a constant angle (45°), while the angle of incidence was varied from 45° to 75°, with 5° steps. Through the *CompleteEase* software, the data was fitted to a Tauc-Lorentz model and the optical properties and thicknesses were determined. In the Annex I, Figure I.1 shows the model structure used for the fitting of the acquired data. Figures I.2 and I.3 show the fitting for films of SiO_xN_y and IGZO, respectively, using the *CompleteEase* software.

3.4 FDTD Simulations

Using the *Lumerical* software, optical FDTD simulations were carried out to obtain the optimized solution for the conductive and non-conductive periodic structure of the cladding. This software is a numerical method that obtains solutions to complex 2D and 3D structures by directly solving Maxwell's curl equations (see Equations 3.1, 3.2 and 3.3). In addition, this method grants real-time representations of the electromagnetic field [30, 31].

$$\frac{\partial \vec{D}}{\partial t} = \nabla \vec{H} \tag{3.1}$$

$$\vec{D}(w) = \epsilon_0 \epsilon_r(w) \vec{E}(w) \tag{3.2}$$

$$\frac{\partial \vec{H}}{\partial t} = -\frac{1}{\mu_0} \nabla \times \vec{E} \tag{3.3}$$

where $\epsilon_r(w)$ is the complex relative dielectric constant, while $\vec{H}$, $\vec{E}$ and $\vec{D}$ are the magnetic, electric and displacement field, respectively.

Since the structure is periodic, the FDTD region was reduced to only one period. Half-periods of 3 μm, 1 μm, 500 nm, 250 nm, 50 nm and 25 nm were simulated.

The wavelength of the light used in the simulations is 532.5 nm. Perpendicular and angular injections of light were simulated. For the perpendicular incidence, periodic boundary conditions (BC) in the x-direction were considered, since the structure and the injected light are both periodic. For the angular incidence, Bloch BC were specified in the x-direction, as both the structure and injected light are periodic, but there's a phase shift between each period. These BC should be considered when electromagnetic fields are injected into the periodic structure at a certain angle [30]. Electromagnetic far-field projections were then plotted and will be discussed later.

Figure 3.3 shows the schematic of the simulated structure on *Lumerical* software for perpendicular (Figure 3.3a) and angular (Figure 3.3b) injections.

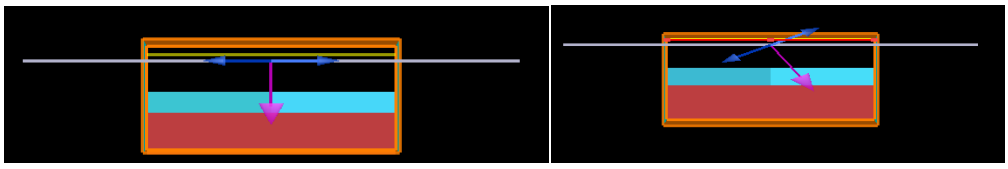

(a) (b)

Figure 3.3: Schematic of the simulation structure for (a) perpendicular and (b) angular injected light.

In this chapter, the results of this work will be presented and discussed, with accordance to the main goal of the project. This study focuses on the creation and development of a-IGZO-SiO_xN_y trenches. The ultimate aim is to optimize both materials to have almost identical refractive indices in the visible range. This way, the light traveling along the core won't suffer any deviation. Moreover, if the size of the trenches is successfully reduced to sub-wavelength, it will expectantly lead to the creation of a metamaterial.

Initially, films of a-IGZO were deposited on top of *Si* wafers. An optical characterization is then conferred. Next, the optimization process of the patterning of a-IGZO layers is presented, as well as its topographical and optical characterization. After determining and optimizing a-IGZO, films of SiO_xN_y were deposited on *Si* wafers. Accordingly, its optical properties are discussed and compared to of the a-IGZO. This is followed by a FDTD simulation of the envisioned structure.

4.1 Grating Structure

4.1.1 a-IGZO Deposition

The first step in the creation of an alternating conductive/non-conductive metamaterial was to deposit 100 and 200 nm thick planar a-IGZO layers on top of *Si* wafers. Before starting the processing on the wafers, SE measurements were carried out to probe the layer's optical characteristics. As stated in Section 2.2, the theoretical refractive indices for a-IGZO in the visible range are, typically, in the range of $1.8 - 1.9$. Figure 4.1b shows the fitted results of the in-house sputtered a-IGZO films, of which the values appear to be higher than in literature, mainly falling in an interval between $2.20 - 1.98$ for visible light.

As stated in Section 2.4.2, it is essential to choose an appropriate optical model in order to accurately extract the optical parameters from a SE measurement [20]. Here, the Tauc-Lorentz model was used, as it has been reported to be a good fit for amorphous semiconductors and insulators [32].

In this model, Equation 2.5 is used to determine the imaginary part of the dielectric function, ε_{2TL}. During the fitting, the peak transition, E_0, was kept fixed at the UV region, with a minimum value of 6 eV, which corresponds to a wavelength of 206 nm.

ε_{2TL} can assume two functions, depending on the energy of the incident light. For energies below the a-IGZO energy bandgap, E_g = 3.5 eV or 354 nm, ε_{2TL} is zero [20]. This is presented in Figure 4.1b, as the extinction coefficient shows an exponential increase as it approaches the

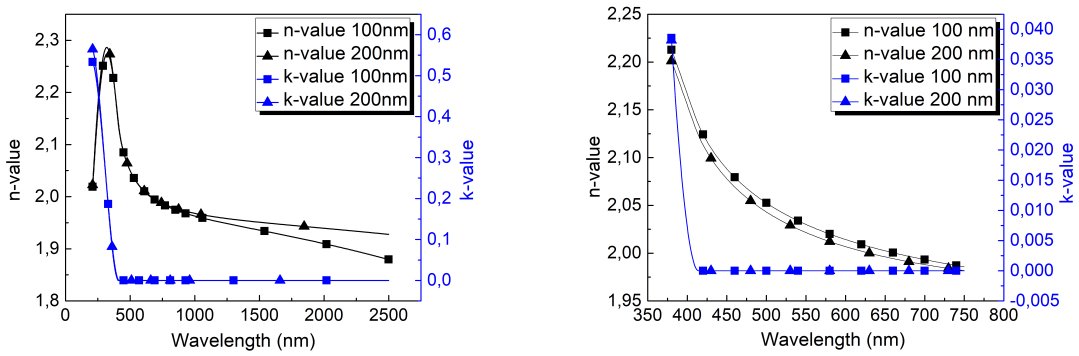

(a) (b)

Figure 4.1: Variation of the refractive index and the extinction coefficient over the wavelength range of (a) 210 – 2500 nm and (b) the visible range, 380 – 750 nm, on 100 nm and 200 nm of a-IGZO films. Optical properties deduced from the Tauc-Lorentz model after being collected by SE.

bandgap energy. Since the extinction coefficient is directly related with the absorption coefficient, this confirms how the incident light is being absorbed in the specific zone where the oscillator is moving at resonant frequencies [20].

When studying Figure 4.1a, as the energy of the incident light increases and reaches the resonant frequency of the fixed oscillator, maximum peaks of the refractive index can be observed. Their values are 2.27 (at 322 nm) and 2.29 (at 319 nm) for 100 and 200 nm, respectively. Both peaks are situated in the near-UV region (315 – 380 nm), which is an indication of the existence of an electric polarization, typical of this region [20].

SE measurements were performed at various angles of incidence, from 45° to 75°, with 5° steps, in order to achieve precise fitting and minimize its error. As mentioned in Section 2.4.2, the MSE values are a good indication of how well the data fits into the used model [26, 33]. A maximum acceptable MSE of 25 was picked, as this error is an indication of how accurate the fittings are. The accomplished MSE values were 22.3 and 19.4, for 100 and 200 nm, respectively.

Next to the optical properties, SE measurements were also used to assess the uniformity of the deposited films. Figure 4.2 shows the surface mapping of the 100 and 200 nm a-IGZO films on top of 200 mm wafers. A clear pattern can be observed in the film thickness. In this sputtering process, there is not a random distribution of the thickness, but instead, a well-reproducible linear distribution. This can be explained by the fact that the O_2 passes are performed horizontally, from the left to the right direction. Hence, its uniformity is fairly good horizontally, but its thickness is poorly distributed vertically. Moreover, the thickness decreases from the bottom to the top of the wafer. This can be explained by the fact that the bottom part is placed closer to the target, which is located in the center of the chamber. Therefore, it has more deposited material than at the top.

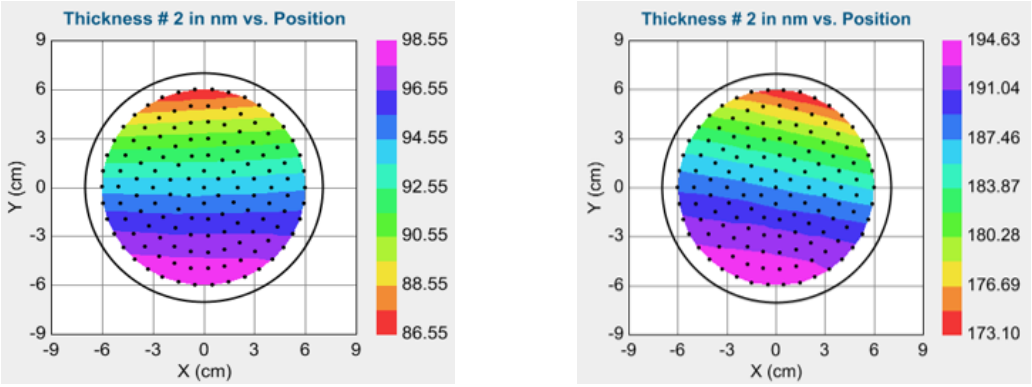

(a) (b)

Figure 4.2: Study on the uniformity of the (a) 100 nm and (b) 200 nm a-IGZO films deposited by PVD. Data extracted from CompleteEASE software [26].

4.1.2 Patterning of a-IGZO

After its characterization, conventional photolithography and etching processes were performed to fabricate the patterned a-IGZO of 100 and 200 nm films. Wet etching was executed with 5 % oxalic acid. Notice that the etch rate of a-IGZO deposited by DC sputtering, for this concentration of oxalic acid is reported to be 40 nm/min [27]. Since the appropriate etching conditions were unknown, different etch times were tested, as summarized in Table 3.3.

As mentioned in Section 3, a mask was designed, which contains five different grating sizes. Even though there is an interest in obtaining the highest resolution possible, the photoresist used in this process, $IX845G$, has a limited resolution of $1.5-2$ μm. As the grating size of the $F5$ region is 1 μm, only the results of the $F4$ region (grating size of 3 μm) are discussed for this photoresist.

The next step was to collect the a-IGZO optical properties after undergoing the photolithographic and etching processes, as well as determining the appropriate etch time for 100 and 200 nm a-IGZO layers. For this, all samples were characterized by SE. Although the latter is one of the most precise and accurate characterization techniques, it is also fully dependent on a suitable optical model to perform a correct fitting of the data. This can lead to some misinterpretation. In order to confirm the obtained results, AFM and profilometry were also carried out [32].

4.1.2.1 100 nm a-IGZO films

The etched regions of the patterned 100 nm a-IGZO samples were first characterized by SE. Figure 4.3a shows the variation of the refractive indices within the wavelength range of $210-2500$ nm for all samples. Figure 4.3b shows the variation of the extinction coefficients of each sample. For comparison purposes, the sample that didn't undergo the photolithographic and etching processes was also plotted in both graphs. Additionally, the MSE values are presented in Figure 4.3b. Notice that all samples present a MSE lower than 25.

When observing the refractive index of these samples, plotted on Figure 4.3a, it is noticeable how it decreases with the etch time. One can also note how the curve of the sample that underwent $3:30$ min of wet etching is very different than the others. While the curves of the samples with

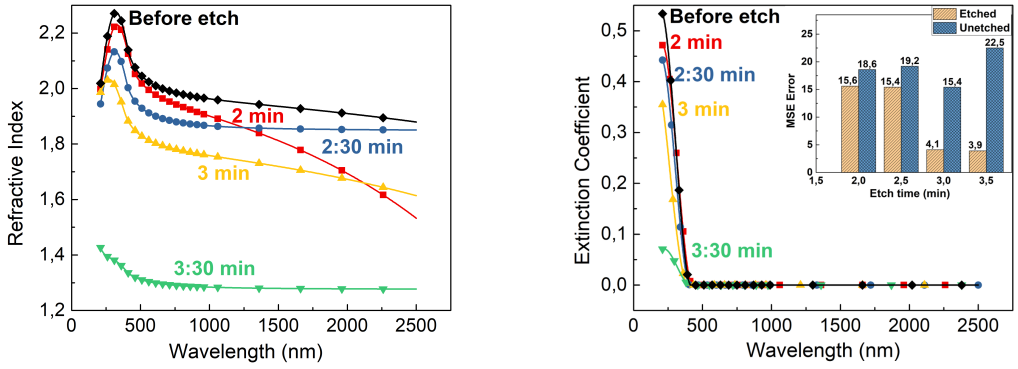

(a) (b)

Figure 4.3: SE fitting results for the 100 nm a-IGZO samples within the wavelength range 210–2500 nm. The deduced refractive indices with the Tauc-Lorentz model are shown in (a) and the extinction coefficients and measure associated MSE values are shown in (b).

less etch time are consistent with the comparison sample, 3 : 30 min of etch seems to be sufficient to completely etch the a-IGZO. Therefore, the refractive index seen in the green curve is from a different material.

An interesting remark can be made about the unusual refractive index curve of the 3 : 30 min etch sample. According to some papers [34, 35], the typical refractive index of a native SiO_2 layer is 1.45 at 633 nm. However, at this wavelength, the material is found to have a n-value of 1.30, which is the stated value of porous SiO_2 [36]. The latter might have been formed during the etching procedure.

Figure 4.3b shows the extinction coefficient values for all samples. This value should be as close to zero as possible, as one wants to eliminate or, at least, minimize the absorption of light in the cladding. SE cannot read values below 10^{-2}, so it is impossible to confirm that k is null. Even though it comes very close, it is crucial to determine the actual value of the extinction coefficient.

As it is fundamental to confirm the SE results, AFM was carried out. One can observe the topographical and $3D$ images of the F_4 region (3 μm) of each sample on Figures 4.4 and 4.5, respectively. All samples present a grating of excellent quality, with little roughness. This is an indication that the used photoresist is appropriate to pattern 100 nm of a-IGZO with gratings of 3 μm resolution.

Profiles were extracted along arbitrary lines for each sample, as there's an interest in determining their average profile heights. These values can be seen in Figure 4.5 for every sample, next to their respective 3D image. When carefully studying these AFM results, one can point out 3 : 30 min to be the appropriate etch time for 100 nm of a-IGZO, as its average profile height is the closest to 100 nm. As the etch time is being increased, the average profile height is becoming closer to 100 nm. If the profile height is less than the thickness of the film, it is an indication that the sample is still underetched.

After confirming that the SE data is consistent with the AFM results, a profilometer was used

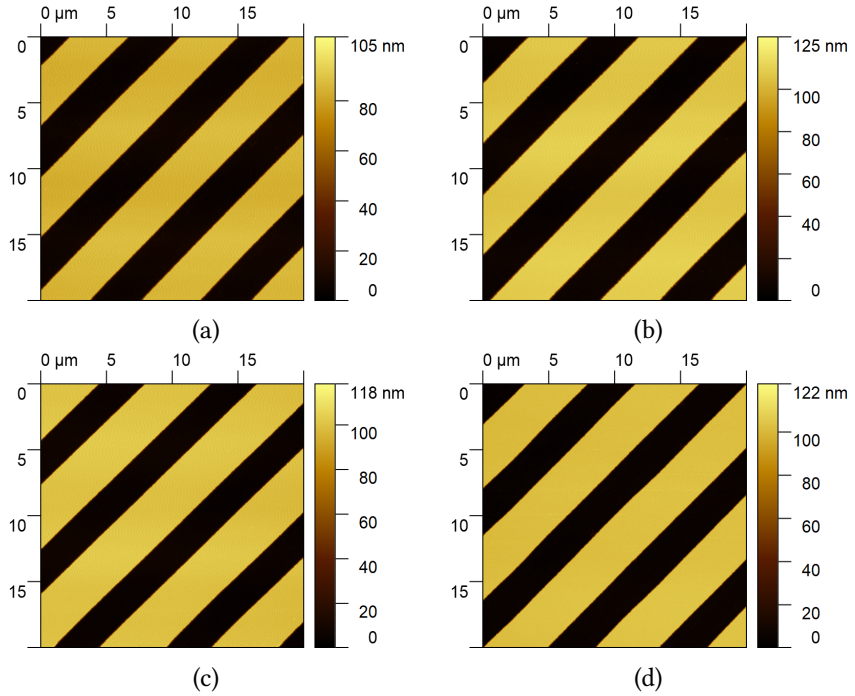

Figure 4.4: Topographic AFM images of 20×20 μm size of the 3 μm grating, $F4$, of samples after (a) 2 min etch, (b) 2 : 30 min, (c) 3 min and (d) 3 : 30 min.

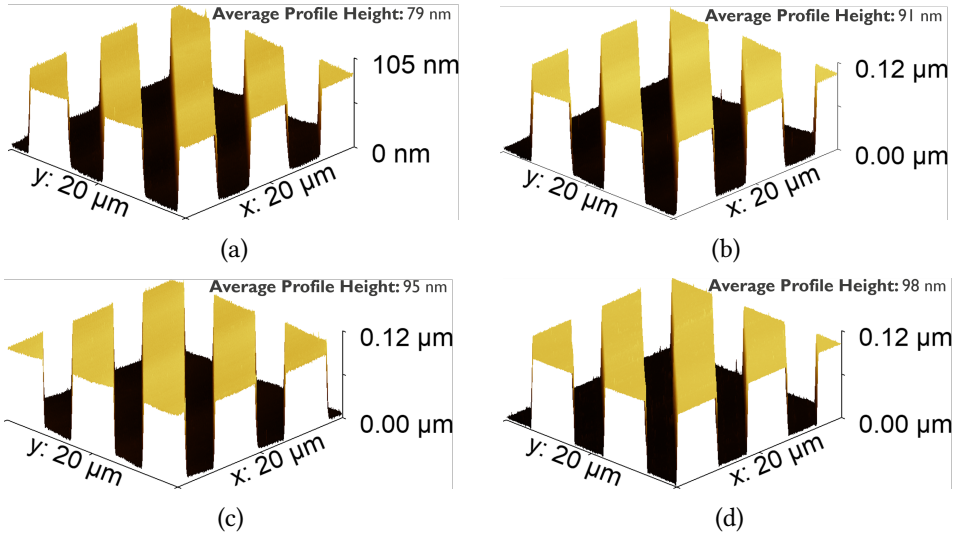

Figure 4.5: 3D AFM images of 20×20 μm size of the 3 μm grating, F4, of samples after (a) 2 min etch, (b) 2:30 min, (c) 3 min and (d) 3:30 min.

to acquire the profiles of each sample. Figure 4.6 compares the etch depth values measured by the three different characterization methods. In Table 4.1, the average between the different acquired etch depths, for each etch time, are represented. Their standard deviation is also shown. As seen in Figure 4.6, as the etch time is increased, the values collected by the different methods come close to each other. This statement can be further backed up by the decrease of the standard deviation as the etch time increases (Table 4.1). Since for the longest etch time the obtained etch

depth is the closest to the desired one, and due to the fact that for this etch time the standard deviation is the lowest, a 3 : 30 *min* etch time is the appropriate for producing the etch of 100 *nm* of a-IGZO.

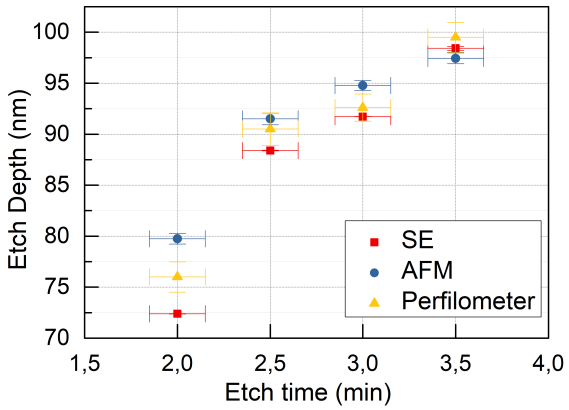

Figure 4.6: Comparison between the etch depth values measured by SE (plotted with red squares), by AFM (plotted with blue circles) and by the profilometer (plotted with yellow triangles). Vertical error bars for the AFM and the profilometer measurements were calculated assuming a 95% confidence interval (number of samples: 30). For the SE they represent the associated MSE error. Horizontal error bars represent errors associated with the etching process, which was considered ±10 seconds.

Table 4.1: Mean etch depths for the 100 *nm* a-IGZO samples, as well as their standard deviation.

	Etch time			
	2 min	2:30 min	3 min	3:30 min
Etch Depth Average ± σ (nm)	76.04 ± 3	90.13 ± 1.29	93.37 ± 1.26	98.45 ± 0.84

4.1.2.2 200 nm a-IGZO films

In this section, all samples underwent the same characterization process as the 100 *nm* a-IGZO films. Hence, the discussion is organized in a similar way.

As mentioned in Section 4.1.2, the etch rate of a-IGZO deposited with DC sputtering, with 5 % oxalic acid, is 40 *nm*/*min*. For this reason, it was expected that 100 *nm* and 200 *nm* of a-IGZO would be completely etched after 2 : 30 min and 5 min, respectively. Although, wet etching is a challenging process and is extremely dependent on the process conditions. Hence, practical results aren't always consistent with the values found in literature. In order to economize some time, a 6-inch *Si* wafer was cut in four pieces and each was etched with different times, as represented in Figure 4.7. When inspecting the wafer, it is noticeable by its blue coloring that 5 min etch is not enough for a-IGZO films of 200 nm. Since with a 7 min etch the wafer presents a yellow color and with a 9 min etch, it presents its *Si* characteristic color, then it can be concluded that the etch time should be between 7 − 9 min.

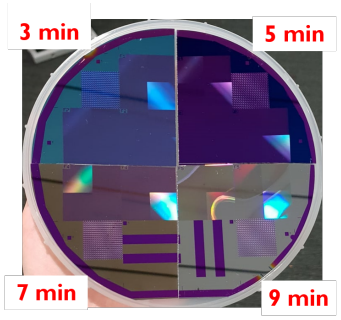

Figure 4.7: Image of a 6-inch *Si* wafer with 200 *nm* of a-IGZO deposited on top after the photolithographic and etching processes. The wafer was cut in four pieces and etched at different times: 3, 5, 7, 9 *min*.

Similar to the SE results for the 100 nm a-IGZO samples, Figure 4.8a represent the variation of the refractive index and Figure 4.8b the extinction coefficient for all samples, as well as their associated MSE values. Note that all MSE values are below 25.

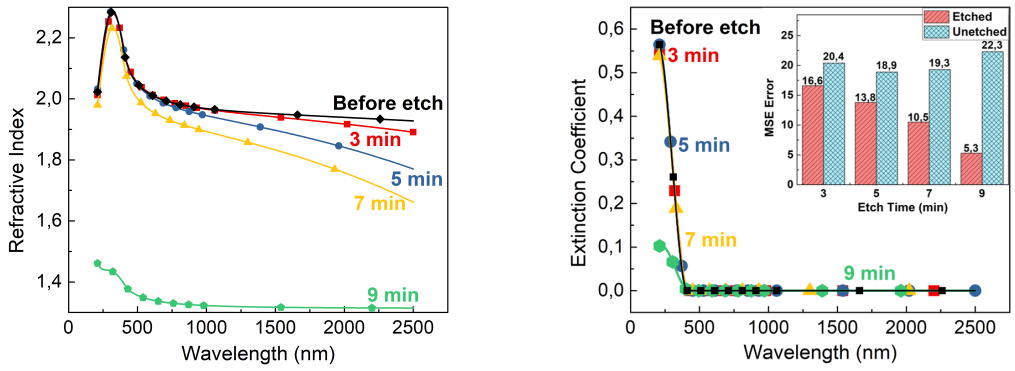

(a) (b)

Figure 4.8: SE fitting results for the 200 nm a-IGZO samples within the wavelength range 210–2500 nm. The deduced refractive indices with the Tauc-Lorentz model are shown in (a) and the extinction coefficients and associated MSE values are shown in (b).

As mentioned for the 100 nm films, the refractive index decreases with the etch time (Figure 4.8a). It also is very distinct how the sample that underwent 9 *min* of etch has a very similar curve to the 100 *nm* a-IGZO sample that underwent 3 : 30 *min* of etch. This suggests that the a-IGZO film was almost completely etched in the process and that porous SiO_2 was again formed. Figure 4.9 shows the refractive index curves for both these samples and it is perceptive how their behavior is very similar.

Figure 4.8b shows the extinction coefficient values for all samples, which are comparable to the 100 *nm* a-IGZO samples. Although SE has a limit read value and there's not a way to confirm that these values are null, they come very close. Further measurements should be carried out to fully determine these values.

The AFM results are shown below. The topographic and 3D images of each sample are

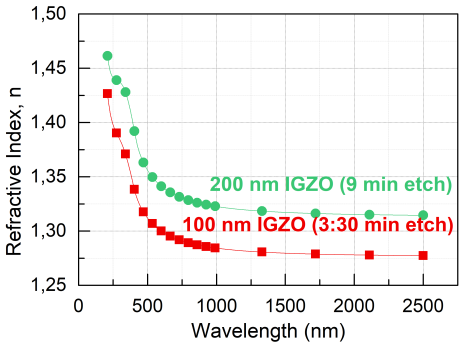

Figure 4.9: Variation of the refractive index over the wavelength range 210 – 2500 nm of the 100 nm a-IGZO sample that went through 3:30 min of etch (plotted with red squares) and of the 200 nm a-IGZO sample that endured 9 min of etch (plotted with green circles).

represented on Figures 4.10 and 4.11, respectively. For these AFM images (Figures 4.11a, 4.11b and 4.11c), some fluctuation is visible, which is an artifact. The latter can be either related to the scanning or the image processing.

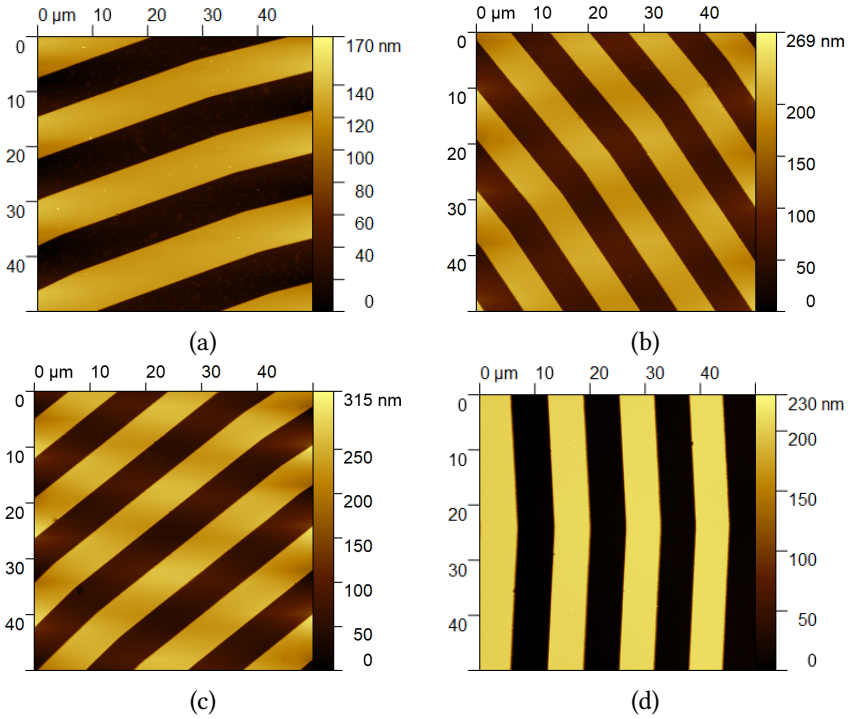

Figure 4.10: Topographic AFM images of 50×50 μm size of the Fresnel lenses region, of samples after (a) 3 min, (b) 5 min, (c) 7 min and (d) 9 min ecth.

Profiles were also extracted along arbitrary lines for each sample, in order to collect their average profile heights. The values are collected in Figure 4.11 for every sample, next to their respective 3D image. According to this data, a 9 min etch is the appropriate time to perfectly etch this thickness of a-IGZO, which is in agreement with the SE results.

Although 9 min seems to be the adequate etch time for the Fresnel lenses region, as shown

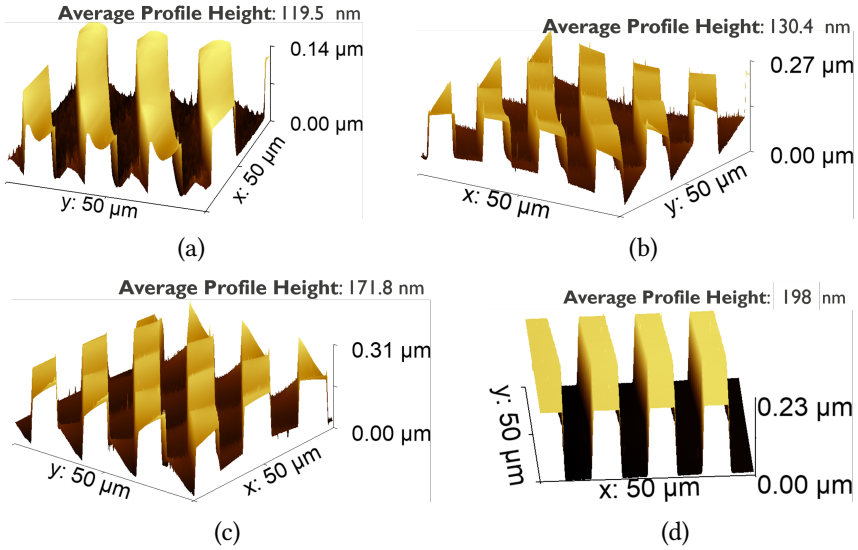

Figure 4.11: 3D AFM images of 50×50 μm size of the Fresnel lenses region, of samples after (a) 3 min etch, (b) 5 min, (c) 7 min and (d) 9 min.

in Figure 4.11d, this should be confirmed for the $3\mu m$ features ($F4$ region). Two 200 nm a-IGZO samples were prepared and 8 min and 9 min of etch were performed. Figure 4.12 presents the topographic images of this region for 8 min (Figure 4.12a) and 9 min (Figure 4.12b) of etch, as well as their respective 3D images (Figures 4.12c and 4.12d). Profiles were also extracted for these samples and according to their average profile heights, stated in Figures 4.12c and 4.12d, 9 min is the proper etch time.

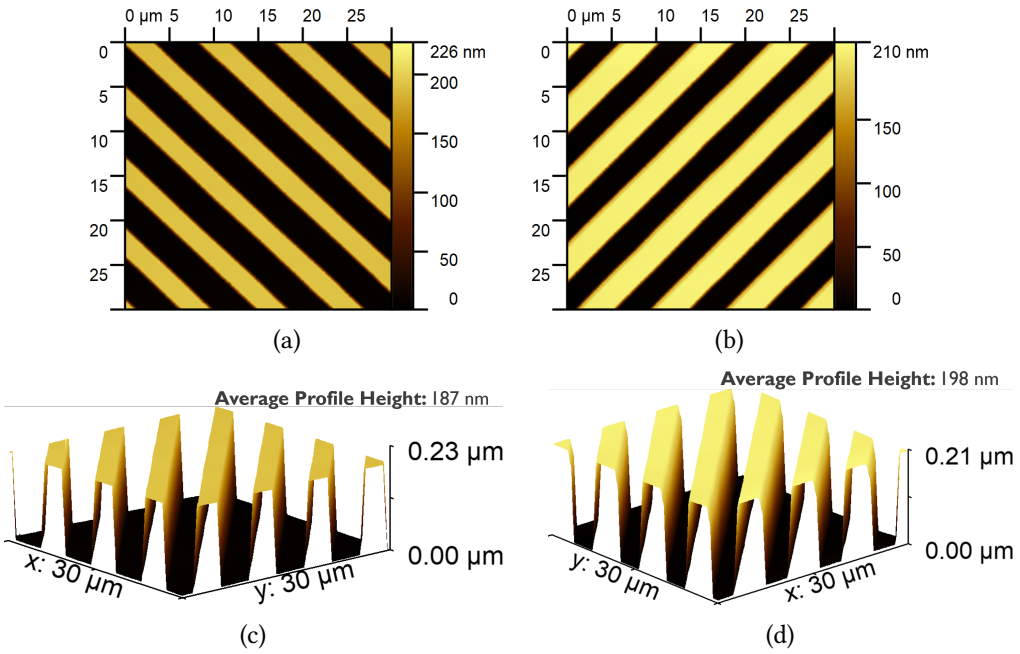

Figure 4.12: Topographic AFM images of 30×30 μm size of the 3 μm grating, $F4$, of samples after (a) 8 min and (b) 9 min etch, and their respective 3D images (c) 8 min and (d) 9 min.

As it was executed for the prior thickness, after confirming that the SE data is congruent with the AFM results, a profilometer was used to collect the profiles of each sample. Figure 4.13 compares the etch depth values measured by the three different characterization methods. Similar to the 100 nm a-IGZO films, with the increase of the etch time, the data of the three methods become closer. To certify this trend, their standard deviations were determined and represented in Table 4.2. The average etch depth is also presented for every sample. For 200 *nm* of a-IGZO, it can be concluded that 9 *min* is the optimized etch time.

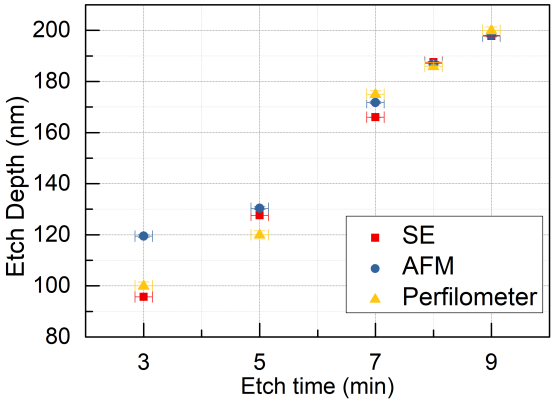

Figure 4.13: Comparison between the etch depth values measured by SE (plotted with red squares), by AFM (plotted with blue circles) and by the profilometer (plotted with yellow triangles). Vertical error bars for the AFM and the profilometer measurements were calculated assuming a 95% confidence interval (number of samples: 30). For the SE they represent the associated MSE error. Horizontal error bars represent errors associated with the etching process, which was considered ±10 seconds.

Table 4.2: Mean etch depths for the 200 nm a-IGZO samples, as well as their standard deviation.

	Etch Time (min)				
	3	5	7	8	9
Etch Depth Average ± σ nm	105.08 ± 10.35	126.00 ± 4.39	170.93 ± 3.72	186.86 ± 0.65	198.93 ± 0.64

4.1.2.3 Optimization of 1 μm features

There is an interest in downsizing the grating size, as this is necessary to manipulate the electric fields with extreme precision through the cladding structure. Although the optimized size of these pillars is expected to be in the sub-wavelength scale, as mentioned in Section 2.2, the optimization should start with larger sizes and carefully reduce it. The available resist (*IX 845G*) had a limited resolution of 1.5 to 2 μm features. In the meantime, a group of fellow colleagues developed and optimized a new recipe that uses a different photoresist (*AZ ECI* 3012). The latter allows features of smaller sizes: 0.6 to 0.8 μm. Since it was a completely different recipe that utilizes a different spinner and exposure type, there is a necessity in optimizing the etch time.

Layers of a-IGZO with 230 nm of thickness were deposited on *Si* wafers. It was decided to perform a 9 min etch, using the old resist on one sample and the new one on another. The 1 μm grating size, $F5$ region, of both samples was characterized by AFM and SE. Both characterization methods indicate that 9 min is the perfect etch time for both resists. According to the SE results, the old resist sample has a native SiO_2 thickness of 2.18 ± 0.02 nm, while the new resist sample has 1.87 ± 0.14 nm. Hence, the added 40 nm of a-IGZO seems to be irrelevant even though, according to the theoretical etch rate of a-IGZO (40 nm/min), an additional minute should be needed to completely etch the a-IGZO. The average profile heights extracted from the AFM images for the old and the new recipes samples are 228 nm and 230 nm, respectively. These measurements are in agreement with the SE results.

AFM height profiles were measured and are represented in Figure 4.14. Although both samples seem to be completely etched with 9 min, there is an interest in maintaining the size of the etched region equal to the size of the a-IGZO pillars for reliability reasons. The new recipe allows the pillars to be slightly taller and larger. When observing the blue profile, there is a meager bump present in all pillars. This might be an AFM artifact and it leads to the believe that the pillars might be even larger than represented here.

In Figure 4.15, the topographic as well as the 3D images of the old and the new recipe samples are represented. These images show the 1μm grating region, $F5$. The a-IGZO pillars are much larger when using the new recipe, which supports the prior paragraph. Despite the fact that this study is an advancement on the needed downsizing of the a-IGZO grating, further optimization should be performed, as these results are based on one single sample. This process should, then, be repeated to verify its reproducibility.

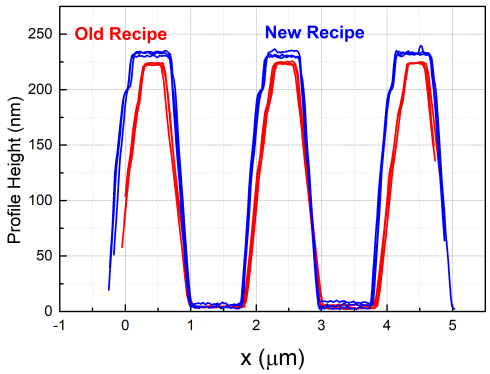

Figure 4.14: Profiles extracted along arbitrary lines for samples that underwent the photolithographic process with the old and the new recipes.

4.2 SiO_xN_y films

After optimizing the a-IGZO grating and determining its optical properties through the use of SE, SiO_xN_y films were deposited on five *Si* wafers. Maintaining the rest of the deposition conditions

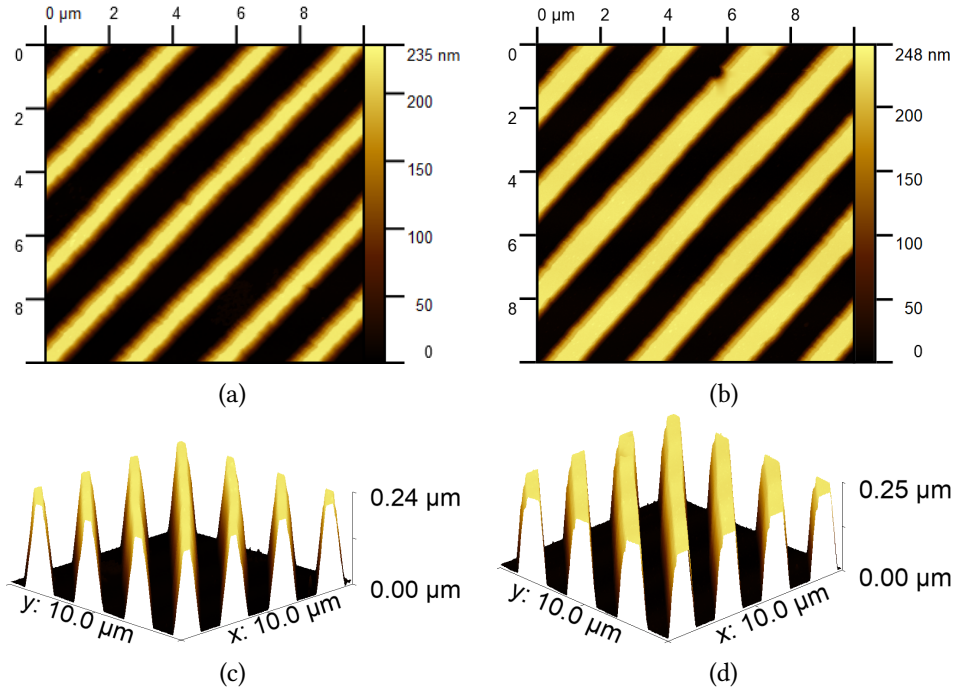

Figure 4.15: Topographic AFM images of 10×10 μm size of the 1 μm grating, F5, of samples that used the (a) old recipe and the (b) new recipe, as well as their respective 3D images, (c) and (d).

constant, the amount of N_2O gas flow rate was increased from 2 – 6 sccm, as seen in Table 3.1.

SE measurements were also used to analyze the uniformity of the deposited films. Figure 4.16 shows the surface mapping of the SiO_xN_y film, deposited with a 4 sccm N_2O flow rate. This sample is representative of the others, since all demonstrate these pattern with different thicknesses. Although, this is not an expected pattern for ICP-CVD deposited films.

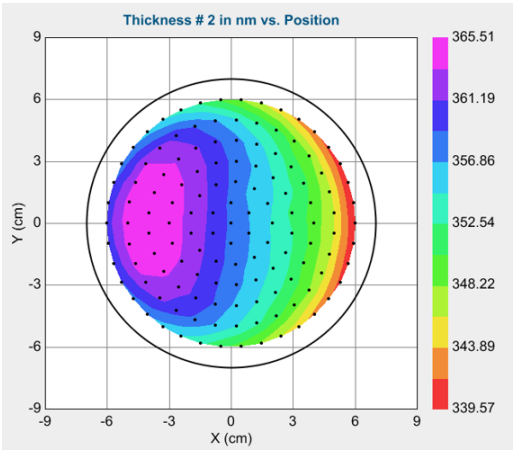

Figure 4.16: Study on the uniformity of a SiO_xN_y film, deposited by ICP-CVD with a 4 sccm N_2O flow rate.

The variation of their refractive indices and extinction coefficients, over the wavelength range of 210 - 1500 *nm*, are represented on Figures 4.17a and 4.18, respectively. Once more, even though the extinction coefficient is nearly close to zero in the visible range, further measurements should

be done to confirm the real value.

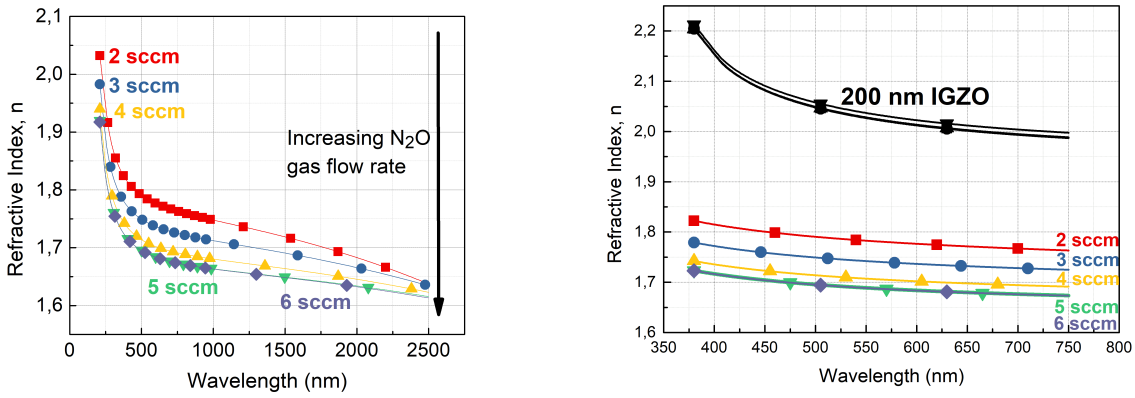

(a) (b)

Figure 4.17: Curves of the refractive index of samples deposited with SiO_xN_y films, with different N_2O flow rates, over the (a) wavelength range 210 - 2500 nm and (b) visible range (380 - 750 nm).

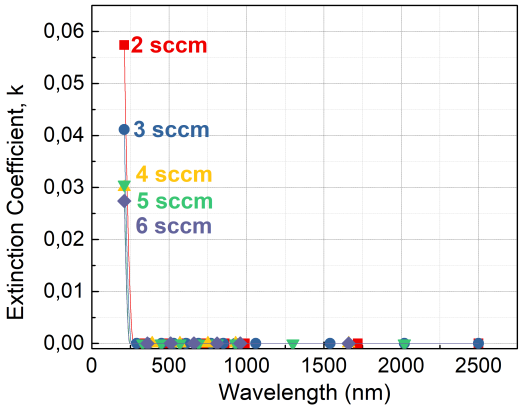

Figure 4.18: Curves of the extinction coefficient of samples deposited with SiO_xN_y films, with different N_2O flow rates, over the wavelength range 210 - 2500 nm.

Figure 4.17a shows a decrease in the refractive index values when increasing the N_2O gas flow rate. Hence, when the amount of this gas is increased, the refractive index of SiO_xN_y becomes further away from of the a-IGZO, which is undesirable. The ultimate aim of this study is to obtain almost equal refractive index curves for both materials, over the visible range. This is not accomplished by increasing N_2O during the SiO_xN_y deposition process, as it can be confirmed in Figure 4.17b.

In a previous study [37], films of SiO_xN_y and Si_3N_4 were deposited on Si wafers with the gas flow rates shown in Table 4.3 [37]. Its optical properties were determined by SE. In the visible range, the refractive indices for SiO_xN_y and Si_3N_4 fall mainly in the intervals between $2.14 - 2.02$ and $2.02 - 1.97$, respectively. These values are much closer to the a-IGZO refractive index values

Table 4.3: Gas flow rates used in [37] in order to achieve films of SiO_xN_y and Si_3N_4.

	Gas Flow Rate (sccm)		
Films	SiH_4	N_2	N_2O
SiO_xN_y	16.8	6.3	4.0
Si_3N_4	16.8	13.3	0.0

(2.20 − 1.98). Furthermore, in the future, reducing the N_2 flow rate to 6.3 sccm or using solely Si_3N_4 should be considered.

4.3 FDTD Simulations

It is important to predict how the IGZO/SiO_xN_y cladding structure behaves with the light traveling inside the core. Hence, FDTD simulations were carried out. Although there is an interest in having the two materials with equal refractive indices, this hasn't been achieved yet. Figure 4.17b shows the obtained refractive indices of IGZO and SiO_xN_y in the visible range. At 532.5 nm, n is 2.04, for a-IGZO, and 1.69 - 1.79, for SiO_xN_y. Therefore, in this simulation, a $n = 2.04$ was used for a-IGZO and a $n = 1.79$ was used for SiO_xN_y. It corresponds to a N_2O flow rate of 2 *sccm*, as it is the closest to the a-IGZO refractive index. These practical results were then simulated and compared with a periodic structure containing two materials with equal refractive indices ($n_1 = n_2 = 2$). As mentioned in Section 3.4, the simulated incident light has a wavelength of 532.5 nm.

Figure 4.19 shows the electromagnetic far-field intensity projections for perpendicular (Figure 4.19a) and angular (Figure 4.19b) injections, when interacting with a structure with a half-period of 3 μm. The following figures show the results using perpendicular and angular injections when interacting with a structure with half-periods of 1 μm (Figure 4.20), 500 nm (Figure 4.21), 50 nm (Figure 4.22) and 25 nm (Figure 4.23). It is crucial to have a localized far-field projection, as it confirms how the incident light is reflected in only one direction when encountering the structure. This way the metamaterial is capable to control the injected light in the best possible way. If this happens in this grating structure, it means both materials are behaving as an uniform medium, exhibiting the exotic properties of a metamaterial. It is believed that this is possible when creating a structure with a sub-wavelength period [38]. As said in Section 2.2, the main goal is to create a structure with a half-period between 25 - 50 *nm*. These simulations confirm that a grating with such small sizes will behave as an uniform medium, allowing the localization of the far-field.

All graphs are represented with the same scale for comparison reasons. The theoretical simulations using a grating structure with equal refractive index values $n_1 = n_2 = 2$ are represented in dashed red. It is important to note that, for the theoretical simulations, the maximum far-field intensity has the same value for all perpendicular simulations, even when reducing the period of the structure. This peak can be found at an angle of 0° with a value of $1.2x10^{-3}$ $(V/m)^2$. This is also true for the angular injection and can be found at an angle of 30° with a peak value of

$3.4x10^{-4}\ (V/m)^2$.

Although the following discussion is regarding the perpendicular injection simulations, the same conclusions should the drawn to the angular injection simulations.

When looking at Figure 4.19a, noise can be seen in the practical refractive indices simulation ($n_{IGZO} = 2.04$; $n_{SiO_xN_y} = 1.79$), which doesn't exist in the theoretical simulation. This means that when using a structure with a half-period of 3 μm, the n-values achieved in this study are not sufficiently close to localize the electromagnetic far-field. This is also true when reducing the half-period size to 1 μm and 500 nm (see Figures 4.20a and 4.21a, respectively). Nonetheless, these results are expected, as the period is still above the wavelength of light. Hence, the structure is not expected to exhibit the metamaterial properties.

The targeted sub-wavelength half-periods of 25 nm (Figure 4.23a) and 50 nm (Figure 4.22a) were then simulated. As it was expected, there is no visible noise for the practical results as they show a very localized peak of the far-field. Hence, the discrepancy between the practical and theoretical results starts to be mitigated, proving that, at 532.5 nm, a grating structure containing the practical refractive index values will behave as an uniform medium.

In order to achieve the aimed goal, it is necessary to continue to reduce the size of the grating structure, which will be a challenge due to its high aspect ratio (thickness will be around 500 nm). Another solution could be to optimize both materials to have the same refractive index, hopefully being able to use periods with a bigger size. A third option could be to find a trade-off between the aspect ratio and the refractive indices, which sounds the most viable one.

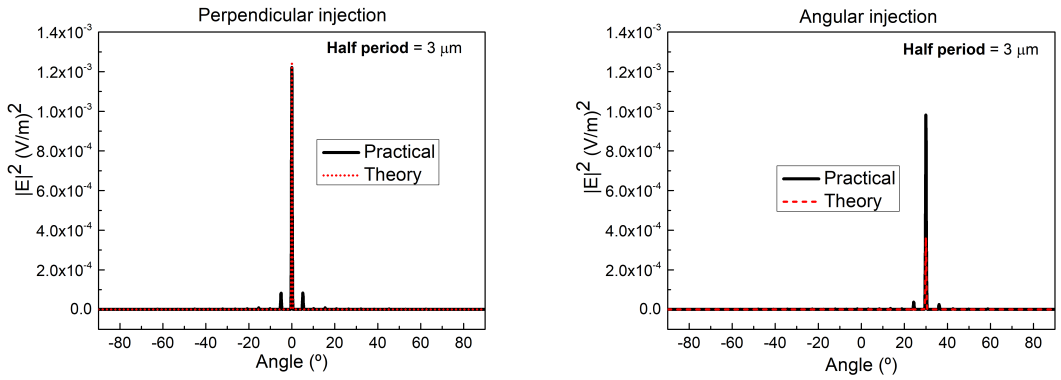

(a) (b)

Figure 4.19: Electromagnetic far-field intensity projections for (a) perpendicular and (b) angular injected light when interacting with a structure with a half-period of 3 μm.

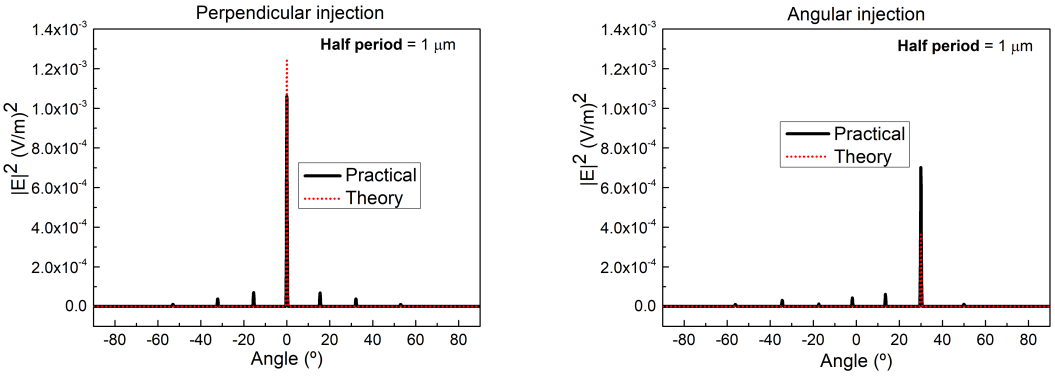

(a) (b)

Figure 4.20: Electromagnetic far-field intensity projections for (a) perpendicular and (b) angular injected light when interacting with a structure with a half-period of 1 μm.

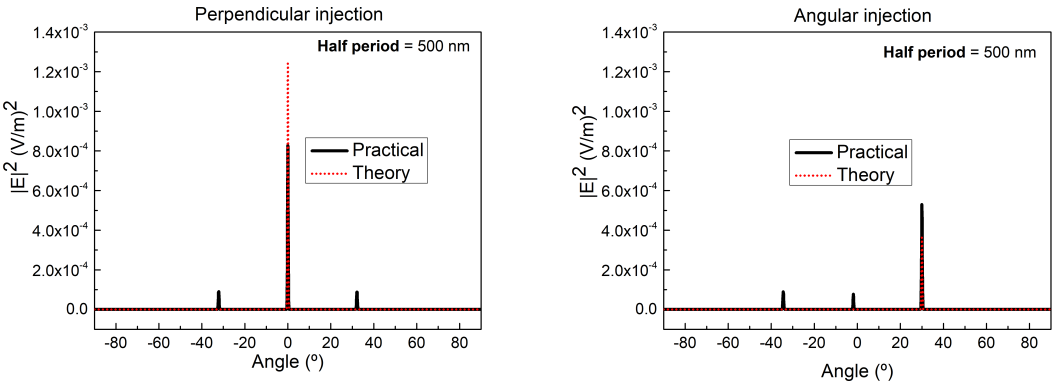

(a) (b)

Figure 4.21: Electromagnetic far-field intensity projections for (a) perpendicular and (b) angular injected light when interacting with a structure with a half-period of 500 nm.

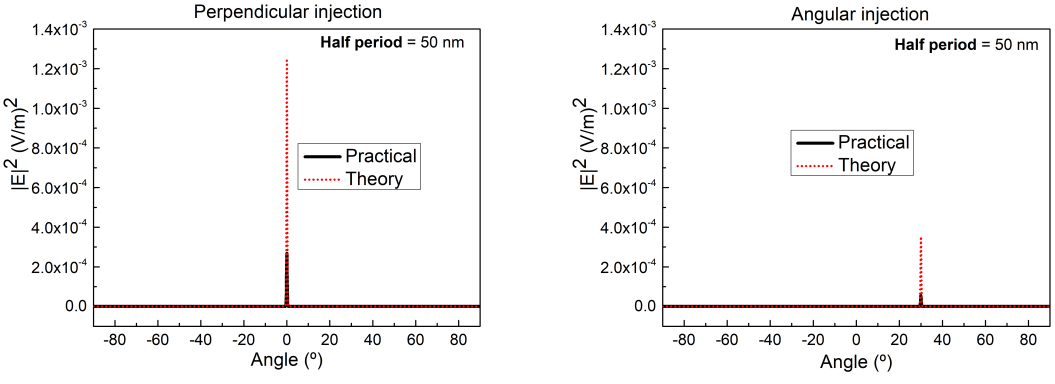

(a) (b)

Figure 4.22: Electromagnetic far-field intensity projections for (a) perpendicular and (b) angular injected light when interacting with a structure with a half-period of 50 nm.

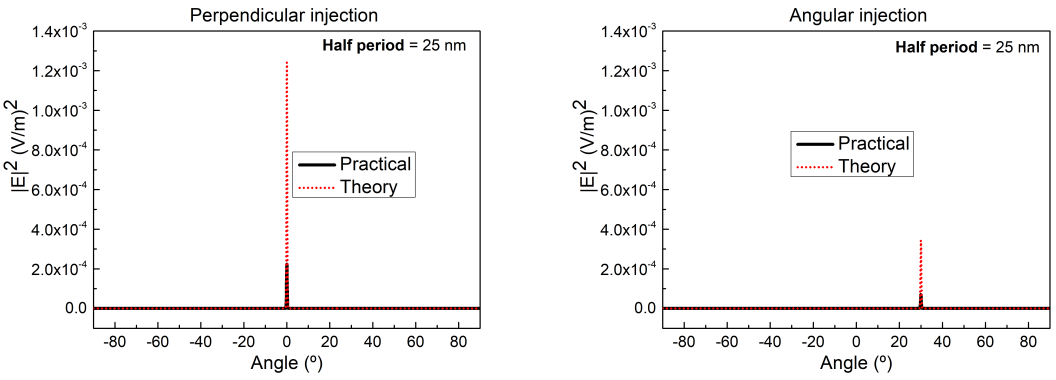

(a) (b)

Figure 4.23: Electromagnetic far-field intensity projections for (a) perpendicular and (b) angular injected light when interacting with a structure with a half-period of 25 *nm*.

Chapter 5

Conclusion and Future Perspectives

The goal of this project was to develop and optimize the cladding composed of a novel metamaterial. Although this hasn't been realized yet, the conductive a-IGZO pillars have been created by optical photolithography. The appropriate etch time, using 5% oxalic acid, in order to create grating sizes of 3 μm and 1 μm, was optimized to 3 : 30 min and 9 min for 100 nm and 200 nm of a-IGZO, respectively.

The refractive indices of a-IGZO and SiO_xN_y were determined over the wavelength range 210-2500 nm. At 532.5 nm, n_{IGZO} is 2.04 and $n_{SiO_xN_y}$ is 1.79, when using a N_2O gas flow of 2 $sccm$. Further optimization is required to reduce the grating size and approximate the refractive indices of both materials. For this, a new optical lithography mask should be designed containing grating sizes in the order of nm. Also, different amounts of N_2O and N_2 should be used, as in Mafalda Calda's work [37], the refractive indices of SiO_xN_y and Si_3N_4 fall in the intervals between 2.14 - 2.02 and 2.02 - 1.97. This proves that the refractive indices of both materials can be matched. If this is achieved, reducing the period of the grating to sub-wavelength sizes, around 25 - 50 nm, might not be necessary for the grating structure to behave as an uniform medium. Although, creating a structure with such small sizes is more desirable, as it offers a much more precise control of the applied electric fields. The extinction coefficients of both materials can be between 0 - 10^{-2}. If it is close to 10^{-2}, it is still an undesirable value, as it will absorb light in a mm or so. In the future, it will be necessary to confirm the real value, since it is expected to obtain an extinction coefficient many orders lower than what the SE can actually measure.

FDTD simulations were carried out to be compared with future practical results of the structure altogether. It was demonstrated that a grating structure with equal refractive indices behaves like an uniform medium for half-periods below or above the used wavelength of light, showing a localized electromagnetic far-field. As the half-periods go to sub-wavelength sizes ($25 - 50$ nm), the simulations using refractive index practical values show a structure behaving as an uniform medium, with very localized far-fields.

Reducing the period of the grating structure should be the main focus of the near future, as the high aspect ratio will be a challenge and will be time-consuming. Further study is needed to match the refractive indices of a-IGZO and SiO_xN_y/Si_3N_4 and to determine the real value of their extinction coefficients.

Bibliography

[1] J. Geng. "Three-dimensional display technologies." In: *Adv. Opt. Photon.* 5.4 (Dec. 2013), pp. 456–535.

[2] *Video-rate holographic projection by novel metameterials.* 2017. URL: https://cordis.europa.eu/project/rcn/210559/factsheet/en (visited on 06/20/2019).

[3] D. Gabor. "Holography, 1948-1971." In: *Science* 177.4046 (1972), pp. 299–313. ISSN: 00368075, 10959203.

[4] S. A. K. Sameer. *Optics and Lasers B. Sc. II.* Kalyani Publishers, 2007. ISBN: 9788127238339.

[5] P. Hariharan. *Basics of Holography.* Cambridge University Press, 2002. ISBN: 9780521002004.

[6] M. Avadhanulu. *A Textbook of Engineering Physics.* S Chand & Company, 1992. ISBN: 9788121908177.

[7] Y. Kong, S. Liu, and J. Xu. "Recent advances in the photorefraction of doped lithium niobate crystals." In: *Materials* 5.10 (2012), pp. 1954–1971.

[8] P. Günter and J. Huignard. *Photorefractive Materials and Their Applications 1: Basic Effects.* Springer Series in Optical Sciences. Springer New York, 2006. ISBN: 9780387251929.

[9] X. An, D. Psaltis, and G. W. Burr. "Thermal fixing of 10,000 holograms in LiNbO3:Fe." In: *Appl. Opt.* 38.2 (Jan. 1999), pp. 386–393. DOI: 10.1364/AO.38.000386.

[10] D. E. Smalley, Q. Smithwick, V. M. Bove, J. Barabas, and S. Jolly. "Anisotropic leaky-mode modulator for holographic video displays." In: *Nature* 498 (2013), pp. 313–317.

[11] P. Tang, D. J. Towner, T. Hamano, A. L. Meier, and B. W. Wessels. "Electro-optic modulation up to 40 GHz in a barium titanate thin film waveguide modulator." In: *Opt. Express* 12.24 (Nov. 2004), pp. 5962–5967. DOI: 10.1364/OPEX.12.005962.

[12] J Kaczmarski, A Taube, E Dynowska, J Dyczewski, M Ekielski, E. Kaminska, and A Piotrowska. "Fabrication and Properties of Amorphous In-Ga-Zn-O Material and Transistors." In: *Acta Physica Polonica A* 124 (Nov. 2013), pp. 855–857. DOI: 10.12693/APhysPolA.124.855.

[13] U. Matebesi, G. Mogosetso, C. K Lebekwe, N. Ditshego, W H Khoo, and S. Mohamed Sultan. "IGZO TFT versus the MOSFET." In: June 2019.

[14] P. West, S. Ishii, G. Naik, N. Emani, V. Shalaev, and A. Boltasseva. "Searching for better plasmonic materials." In: *Laser & Photonics Reviews* 4.6 (2010), pp. 795–808. DOI: 10.1002/lpor.200900055.

[15] A. Galca, G. Socol, and V. Craciun. "Optical properties of amorphous-like indium zinc oxide and indium gallium zinc oxide thin films." In: *Thin Solid Films* 520.14 (2012), pp. 4722 –4725. ISSN: 0040-6090. DOI: https://doi.org/10.1016/j.tsf.2011.10.194.

[16] K. Wörhoff, A. Driessen, P. Lambeck, L. Hilderink, P. Linders, and T. Popma. "Plasma enhanced chemical vapor deposition silicon oxynitride optimized for application in integrated optics." In: *Sensors and Actuators A: Physical* 74.1 (1999), pp. 9 –12. ISSN: 0924-4247. DOI: https://doi.org/10.1016/S0924-4247(98)00325-2.

[17] W. Kim, J. Guo, and J. Hendrickson. "Subwavelength metal grating metamaterial for polarization selective optical antireflection coating." In: *Journal of the Optical Society of America B* 32 (May 2015). DOI: 10.1364/JOSAB.32.001392.

[18] S.-Y. Lee, Y.-H. Kim, S. M. Cho, G. Kim, T.-Y. Kim, H. Ryu, H. Kim, H. Kang, C.-Y. Hwang, and C.-S. Hwang. "Holographic image generation with a thin-film resonance caused by chalcogenide phase-change material." In: *Scientific Reports* 7 (Jan. 2017), p. 41152. DOI: 10.1038/srep41152.

[19] C.-Y. Hwang, G. Kim, J.-H. Yang, C.-S. Hwang, S. M. Cho, W.-J. Lee, J.-E. Pi, J. H. Choi, K. Choi, H.-O. Kim, S.-Y. Lee, and Y.-H. Kim. "Rewritable full-color computer-generated holograms based on color-selective diffractive optical components including phase-change materials." In: *Nanoscale* 10 (Sept. 2018). DOI: 10.1039/C8NR04471F.

[20] H. Fujiwara. *Spectroscopic Ellipsometry: Principles and Applications.* Wiley, 2007. ISBN: 9780470060186.

[21] H. Tompkins and J. Hilfiker. *Spectroscopic Ellipsometry: Practical Application to Thin Film Characterization.* Momentum Press. ISBN: 9781606507285.

[22] H. Radi and J. Rasmussen. *Principles of Physics: For Scientists and Engineers.* Undergraduate Lecture Notes in Physics. Springer Berlin Heidelberg. ISBN: 9783642230264.

[23] D. A. Gonçalves and E. A. Irene. "Fundamentals and Applications of Spectroscopic Ellipsometry." en. In: *Química Nova* 25 (Sept. 2002), pp. 794 –800. ISSN: 0100-4042. DOI: 10.1590/S0100-40422002000500015.

[24] G. Jellison Jr and F. Modine. "Parameterization of the optical functions of amorphous materials in the interband region." In: *Applied Physics Letters* 69.3 (1996), pp. 371–373.

[25] D. Kang, I. Song, C. Kim, Y. Park, T. D. Kang, H. S. Lee, J.-W. Park, S. H. Baek, S.-H. Choi, and H. Lee. "Effect of Ga/In ratio on the optical and electrical properties of GaInZnO thin films grown on SiO_2/Si substrates." In: *Applied Physics Letters* 91.9 (2007), p. 091910.

[26] *CompleteEase Manual, J. A. Woollam Co.* 2011. URL: https://physlab.lums.edu.pk/images/f/f4/Ellipsometry_manual.pdf (visited on 05/21/2019).

[27] M. Nag. "Study of Process Technology and Device Architecture for Amorphous Indium Gallium Zinc Oxide Thin Film Transistors." Doctoral dissertation. KU Leuvens, Dec. 2016.

[28] *Süss Delta 80 spinner technical specifications.* 2012. URL: http://www.bu.edu/photonics/files/2012/06/Delta-80T2-200.pdf (visited on 08/20/2019).

[29] *Controlling Reflectivity and Thin Film Interference in Monochromatic Lithography.* 2013. URL: http://www.imicromaterials.com/technical/reflectivity-control-in-lithography (visited on 08/21/2019).

[30] *FDTD Solutions Lumerical Software Manual.* 2011. URL: https://www.lumerical.com/products/fdtd/ (visited on 05/25/2019).

[31] J. Frances, C. Neipp, A. Marquez, A. Belendez, and I. Pascual. "Analysis of Reflection gratings by means of a matrix method approach." In: *Progress In Electromagnetics Research* 118 (Jan. 2011), pp. 167–183. DOI: 10.2528/PIER11050403.

[32] C Talagrand, X Boddaert, D. Selmeczi, C Defranoux, and P Collot. "Ellipsometry study of process deposition of amorphous Indium Gallium Zinc Oxide sputtered thin films." In: *Thin Solid Films* 590 (2015), pp. 134–140.

[33] T. Oates. "Metal plasma immersion ion implantation and deposition using polymer substrates." In: (2003).

[34] Y. Chen and G. Jin. "Refractive index and thickness analysis of natural silicon dioxide film growing on silicon with variable-angle spectroscopic ellipsometry." In: *Spectroscopy (Santa Monica)* 21 (Oct. 2006), pp. 26–31.

[35] L. V. R. de Marcos, J. I. Larruquert, J. A. Méndez, and J. A. Aznárez. "Self-consistent optical constants of SiO2 and Ta2O5 films." In: *Opt. Mater. Express* 6.11 (Nov. 2016), pp. 3622–3637. DOI: 10.1364/OME.6.003622.

[36] H. Sohn. "Refractive Index of Porous Silicon." In: Jan. 2014, pp. 230–260. ISBN: 978-3-319-04508-5. DOI: 10.1007/978-3-319-04508-5_25-1.

[37] M. Caldas. "Stacks of alternating conductive and non-conductive oxides studied by ellipsometry." Master's thesis. Universidade Nova de Lisboa, Sept. 2018.

[38] X. Zhang and Y. Wu. "Effective medium theory for anisotropic metamaterials." In: *Scientific reports* 5 (Sept. 2014). DOI: 10.1038/srep07892.

Annex

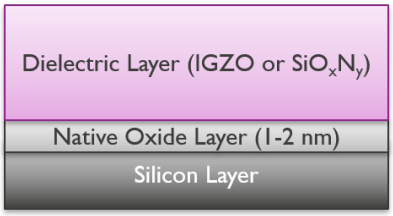

Figure I.1: Model used to perform the fit of the data obtained by *J. A. Woollam Dual Rotating-Compensator (RC2) SE*.

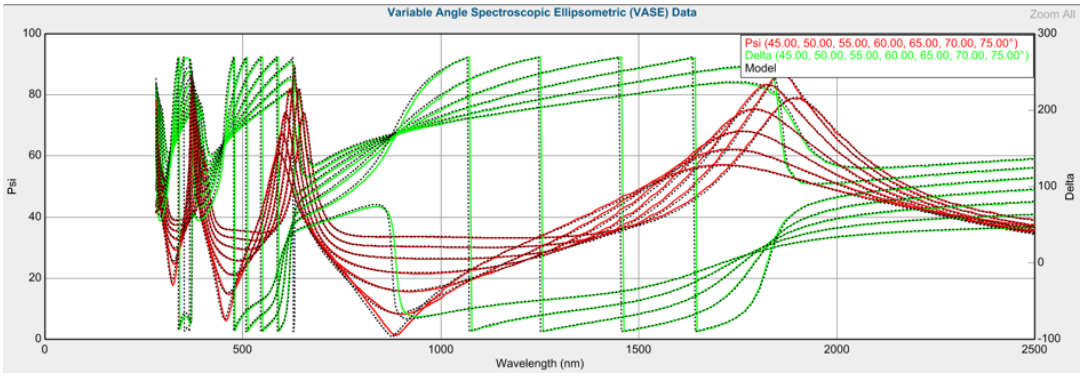

Figure I.2: Fitting of one of the SiO_xN_y samples to the Tauc-Lorentz model using the *CompleteEase* software.

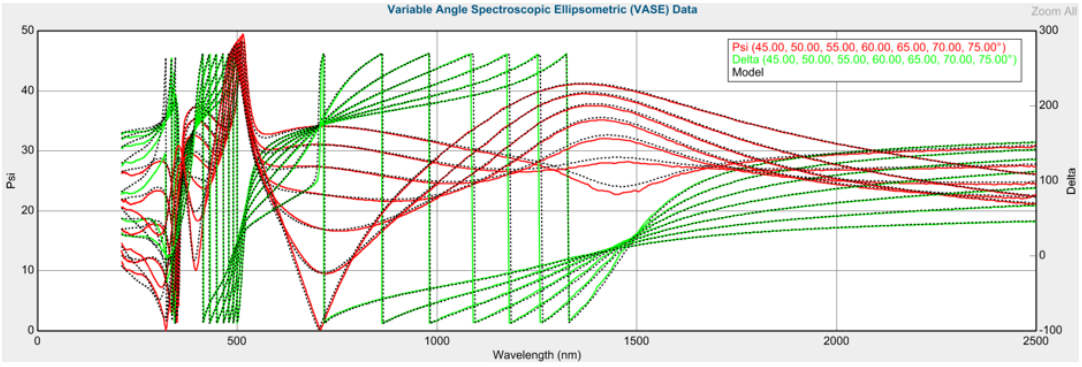

Figure I.3: Fitting of one of the IGZO samples to the Tauc-Lorentz model using the *CompleteEase* software.